Politecnico di Milano

Scuola di Ingegneria Industriale e dell'Informazione

Ingegneria Fisica

Scanning tunneling microscopy study of the growth mechanisms of metal clusters on surfaces

Author:
Gabriele Irde

Matricola:
783450

Supervisor:
Dr. Carlo S. Casari

Co-Supervisor:
Dr. Alexander Khajetoorians
Hamburg University, Hamburg, Germany

Academic Year 2013/2014

Contents

List of Figures

Abstract

New materials properties are of great value for future technology improvement. Nowadays, a lot of efforts are made into miniaturizing devices, and thus, great interest dwells in understanding novel materials, and especially their interactions with supporting substrates. Among these materials, particular attention has to be payed to those with remarkable magnetic and electronic properties even in the nanoscale, thus exploitable for electronics progress. This thesis covers a growth study of Holmium on Iridium and Platinum, and of Iron on Bismuth Selenide, by means of scanning tunneling microscopy. These materials have already been studied extensively, but never in such combinations. All experiments have been performed under ultra high vacuum conditions ($\approx 10^{-12}$ mbar) and at 30 K.

Holmium has been deposited on clean Iridium (111) and Platinum (111) surfaces; no island formation is shown, but clusters whose average size can be tuned by adjusting the deposition temperature, in the Platinum case, and the annealing temperature, in the Iridium case. In addition, Holmium adatoms seem to repel each other until enough energy is given them to cluster together. For high enough coverages in the sub-monolayer regime, Holmium shows hexagonal patches on the Iridium. An additional statistical analysis of the Holmium adatoms distribution has been performed, providing information about its arrangement on the surface, and pointing out a short range order.

Iron has been deposited on Bismuth Selenide cleaved *in situ*, subsequently annealing the sample at temperatures below 300 °C. The presence of smooth islands with a rectangular lattice is observed. The lattice type and its constant are in contrast both with pseudomorphical growth of Iron, and pure Iron islands. No superconductive gap has arisen from STS measurements on the islands.

Abstract

Nel campo della ricerca, e specialmente in ambito tecnologico, riveste particolare interesse lo studio di nuovi materiali. Al giorno d'oggi, vi é uno sforzo considerevole atto alla miniaturizzazione dei dispositivi; per questo motivo, la comprensione delle proprietá di materiali innovativi, ed in special modo delle loro interazioni con i substrati su cui vengono cresciuti, desta un notevole interesse. All'interno di questa classe di materiali, é opportuno prestare particolare attenzione a quelli che presentino peculiari proprietá elettroniche e magnetiche su scala nanometrica, che quindi potrebbero essere utilizzati nel campo dell'elettronica applicata. Questa tesi tratta la crescita di Olmio su superfici di Iridio e Platino, e la crescita di Ferro sul Seleniuro di Bismuto con l'ausilio della spettroscopia ad effetto tunnel. Tali materiali sono giá stati oggetto di vari studi, eseguiti con varie tecniche di indagine, ma mai secondo questi specifici accoppiamenti. In questo lavoro sperimentale, tutti gli esperimenti sono stati svolti in condizioni di ultra alto vuoto ($\approx 10^{-12}$ mbar) ed alla temperatura di 30 K.

L'Olmio é stato depositato sulle superfici pulite Iridio (111) e Platino (111): non é stata riscontrata la formazione di isole sulla superficie, ma bensí, di semplici aggregati atomici di Olmio. É stato inoltre trovato che la dimensione di tali aggregati é regolabile modificando la temperatura di deposizione, nel caso del Platino, e la temperatura di annealing, nel caso dell'Iridio. Inoltre, gli atomi di Olmio, depositati, sembrano repellersi a vicenda sino a quando non viene fornita loro sufficiente energia per formare un aggregato. Per alte coverages nel regime sub-mononolayer, ed in punti particolarmente ordinati del campione, l'Olmio mostra una disposizione esagonale degli atomi adsorbiti sull'Iridio. É stata svolta un'analisi statistica supplementare della distribuzione di tali atomi per ottenere informazioni riguardo il loro arrangiamento sulla superficie; é stato evidenziato un ordine a corto raggio. Il Ferro é stato depositato sul Seleniuro di Bismuto preparato *in situ*, e dunque scaldato sino a temperature inferiori ai 300 °C: si é osservata la formazione di isole con reticolo rettangolare. Il tipo di reticolo, ed il parametro reticolare, escludono la crescita pseudomorfica del Ferro ed anche che le isole in questione siano costituite dal solo Ferro. Non é stata riscontrata alcuna gap superconduttiva nel corso delle misurazioni STS sulle isole.

Introduction

Modern technology in recent years has been focusing on maximizing the performances of computers, chips and electronic devices as a whole in several aspects - memory storage capacity, computational speed, low power consumption and portability. Such demands have led to the progressive shrinking and scaling of the aforementioned devices, down to the nanometric and atomic scale. In facts, smaller dimensions means increasing the storage bytes over the volume of the device by decreasing the size of the single memory unit, means faster signals propagation due to shorter conduction paths and also means that lower currents are needed, so that even the power supply is kept to a minimum. For these reasons, research of fundamental physical properties of materials at the nanoscale has been carried on in several areas. Particular attention has been paid in the last few years to surface science and to its applications.

Nanoislands on surfaces are interesting in several respects: to begin with, their properties are in between atoms and bulk materials, and depending on their size and fabrication conditions one can tune their properties such as electronic behavior, energy levels, magnetic configurations, and transport properties. Besides, their interaction with the substrate open to a wide range of possibilities; the substrate can modify island properties (for example with its surface states or magnetic anisotropy), or merge with the island, hence mixing their characteristics. In my work I concentrated my effort on materials such as Holmium, Iridium, Platinum, Iron and Bismuth Selenide. Holmium is a material with a high magnetic moment, which was proven to have a stable magnetic state even as single atoms at very low temperature onto clean Platinum surfaces. Moreover, Iridium, in combination with Iron, has shown peculiar stable spin configurations, called skyrmions, that can be modified by means of a low current. One could also wonder what would be the outcome of depositing Holmium nanoislands on these materials, given its stronger mag-

netic moment. It is easy to see how these materials could very well be the stepping stone for realization of magnetic information storage units scalable to the nanometric dimension. On the other hand, Bi_2Se_3 is a topological insulator that shows metallic surface states with a linear dispersion, no degeneracy in spin and subject to few scattering events. As a consequence, is a material with potential striking features like low current dissipation, spin selected currents and the possibility to choose current carriers by shifting the Fermi level. In addition, Iron Selenide (FeSe) is a recently discovered high Tc superconductor that, as such, is interesting for lower consumption devices.

Given the significance of this topic, a suitable experimental technique is necessary to investigate the samples. Scanning tunneling microscopy (STM) proved to be an excellent tool to study surface physics since its realization in 1981. Thanks to its exponential dependence of the current on the distance between the sample and the probing tip, STM is capable to obtain information down to the atomic level while scanning on the sample surface. Among its advantages, STM analyzes the topography of scanned surfaces and growth processes, provides insights on electronic structure and magnetic properties, and is also capable to manipulate atoms and molecules to realize complex quantum structures.

The scope of my work was to investigate the growth of Holmium nanoislands on pristine Iridium and Platinum surfaces, and the growth of Iron on Bismuth Selenide. To do so I have deposited the materials by means of molecular beam epitaxy (MBE); hence, I studied the growth mainly by using scanning tunneling microscopy. All the measurements - and most of the sample preparations - have been performed in a ultra high vacuum system (UHV), to ensure the cleanness of the specimens at the atomic level, and at low temperature ($\approx$ 30 K). At last I have analyzed the distribution of Holmium adatoms on Iridium and Platinum surfaces with the aid of a Matlab code developed by the Hamburg University.

This manuscript has been divided in chapters as follows: *Chapter 1* briefly introduces the theory of film and islands growth on surfaces, and presents the materials used in this thesis, as well as their properties and how they have previously been investigated - major attention is paid to STM measurements. *Chapter 2* alights on scanning tunneling microscopy theoretical models and techniques exploited during my work. Subsequently, the UHV system and the most important experimental appliances are described in *Chapter 3*; also, evaporators calibration and tip preparation is shortly summarized. *Chapter 4* exhibits the result of Holmium deposition on Iridium (111) and Platinum

(111) surfaces, and of Iron deposition on top of the Bismuth Selenide. Firstly, sample preparation is explained in each paragraph, then followed by topographies and a discussion of the results. *Chapter 5* focuses on the distribution of the Holmium on the Iridium (111) and Platinum (111) surfaces; after a brief introduction of the code and of the needed statistical theory, the result of the analysis are presented, highlighting the position of the Holmium adatoms and their mutual distances. Finally, *Chapter 6* summarizes the results collected in this thesis, and quickly discusses possible outlooks for deeper insights.

Chapter 1

Deposition of thin films and nanoislands

This chapter introduces the topic of deposition and characterization of thin films and nanoislands on surfaces, and the systems used in this work. First a short theory of growth on surfaces is presented. Later on, is placed a summary of nature and technological properties of the samples - referring to substrates and deposited materials as well. Finally, an overview is given of the existing experimental work on similar systems and the current state of knowledge, paying particular attention to the the results obtained with the same technique exploited in this thesis, namely the scanning tunneling microscopy.

1.1 Growth and characterization

Solids interfaces between thin films and solid substrates have been studied and researched since a long time, but an extensive investigation has been carried on especially over the past few decades. Nowadays they are of major importance in modern technology, and a lot of effort has been spent in developing techniques to implement them. The state of the art focus mainly on epitaxial films that have been grown on crystalline material by Molecular Beam Epitaxy (MBE) [1]. The epitaxial growth of monocrystalline film can be differentiated in *heteroepitaxy* and *homeoepitaxy*; in the first case the substrate material differs from the film's one, while in the last case film and

---

[1]Epitaxy refers to the deposition of a crystalline overlayer on a crystalline substrate.

substrate consist of the same material. In the framework of this project deposited materials have been chosen different from the substrates, thus in this brief theoretical introduction to the surface growth I will refer particularly to the heteroepitaxial growth. Under the assumption of flat surfaces, the growth is based on a thermodynamic equilibrium between surface tensions of the substrate, of the deposited material and of the interfaces between the two. The surface tension is the characteristic free energy (per unit area) to create an additional piece of surface. This concept is easily summarized by the Young-Dupré equation

$$\gamma_s = \cos \alpha \gamma_{dep} + \gamma_i \qquad (1.1)$$

where the γ_s,γ_{dep} and γ_i are respectively the three tension aforementioned, and α is the angle between the substrate surface and the deposited interface (see Figure 1.1). Depending on the fact that $\gamma_i + \gamma_{dep} <$, or $> \gamma_s$, different growth modes are favored. In general, three markedly different modes of film growth can be distinguished:

- *Layer-by-layer* growth, known as Frank-van der Merve mode

- *Island* growth, known as Vollmer-Webber mode

- *Layer-plus-island* growth, known as Stransky-Krastanov mode

In the first the interaction between the substrate layer and atoms is stronger than the one between neighboring layer atoms, resulting from the inequality $\gamma_i + \gamma_{dep} < \gamma_s$ with $\alpha = 0$; each new layer starts to grow only when the last one has been completed. Conversely, the second is characteristic of a stronger interaction between atoms rather than between atoms and substrate, i.e. $\gamma_i + \gamma_{dep} > \gamma_s$, with $\alpha > 0$, and multilayers of conglomerated adsorbed atoms are formed. The last growth mode is an intermediate case; after formation of one or more monolayers, island formation occurs. This can be understood by considering the lattice mismatch between the deposited film and the substrates. Initially the film adapts pseudomorphically to the substrate's lattice at the expense of elastic deformation energy. In the next layers, when the elastic strain filed exceeds the adhesion energy, island growth occurs. However, this model based solely on the Young-Duprè equation is rather simplistic; a lot of factors contribute to decide which of the three modes will result, such as the temperature and pressure, the presence of defects on the surface, and the particular deposition method. Indeed, the surface is not really
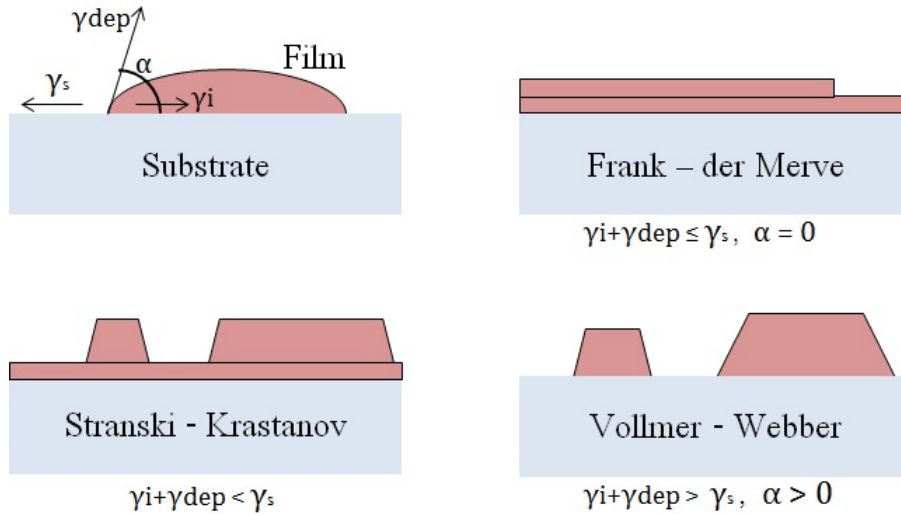
Figure 1.1: Simplified picture of deposited island of a film on a substrate. In the figure are showed the three growth modes and the different surface tensions with the angle α in between.

"flat" but has a rather complex morphology made of adsorbate atoms and impurities, step edges and holes, that altogether contribute to select preferential sites for the nucleation of the deposited material film. In addition, the particular crystallographic direction of the substrate plays an important role too, since it affects the lattice constant on the surface, and thus the lattice mismatch between the substrate and the film.

Regarding the deposition method, on the other hand, the MBE has proved to achieve the best control over thin films growth, especially when combined with the ultra-high vacuum technology. In facts, MBE is a method to prepare fresh, clean epitaxial films in ultra-high vacuum (UHV) by evaporation and condensation of thin films on the substrate's surface. UHV ($\approx 10^{-10}$ mbar) conditions are crucial for epitaxial growth, which needs a substrate surface free of contaminations. The epitaxial film is then given by the interaction of one evaporated beam of atoms or molecules with the crystal substrate.

Standard methods for studying and characterizing the growth of a film in situ are Auger electron spectroscopy (AES) and X-ray photoemission spectroscopy (XPS), since they give quantitative information regarding the chemical nature of the samples. Other well known techniques are the ones based on the diffraction of electrons on the surface, for example RHEED (reflection

high energy electron diffraction) and LEED (low energy electron diffraction), which provide information respectively on the number of monolayers grown and about the large scale lattice ordering (especially useful in the case of different orderings of the substrate and deposited material lattice). A drawback of the aforesaid techniques is that they can describe what is happening on the sample on a global level by averaging over the whole sample. On the contrary, the Scanning tunneling microscopy (STM) yields a "real space" image of the film surface, by exploiting the electron tunneling effect. Its spatial resolution can very well reach the atomic level both laterally and perpendicularly to the surface, granting a more detailed knowledge of the mechanisms and procedures of growth. As an example, it is possible to study the interaction of the deposited atoms both in the monolayer and sub-monolayer regime, to identify the preferred nucleation sites, or to observe any surface reconstruction [2][1]. Also, STM can monitor the growth in a step by step fashion, checking its dependence on pressure, temperature, time exposure to the molecular beam, and several others parameters. Moreover, this probing method can also provide information about the magnetic and electronic properties of the film due to the intrinsic relationship between tunneling current and probed electronic states, as it will be explained in more details in the next chapter.

1.2   Holmium, Iridium and Platinum

Pursuing a more efficient scaling of data storing in the past few years, the magnetism of matter was vastly investigated. During this work we tried to combine different atomic species holding both striking magnetic properties; we used the Iridium and the Platinum as substrates and the Holmium as the deposited material. The Iridium and the Platinum have similar properties and both are highly conducting metals and resistant to oxidation. They have a close cubic packed crystal structure and in both cases the (111) surface is the one that holds the highest scientific interest. Regarding their magnetic properties, the Iridium (Ir), and in particular its (111) surface has drawn a lot of interest due to the discovery of skyrmions [11]. The skyrmions are stable spin configurations which usually originate from chiral interactions known as Dzyaloshinckii-Moriya interactions, and that show a particle-like behavior. Such spin configuration have been found in an atomic thin Iron layer grown on top of Ir(111), and it has been shown that they can be "written" and "deleted" by a spin polarized current injection [23]. On the other hand, the

Platinum has been recently used in combination with Holmium single atoms showing the possibility to obtain stable *atomic* magnetic configuration with lifetimes up to several minutes [21]. Such results are claimed to be due to the interaction between a highly conductive metal, such as the Platinum, and strongly magnetized atoms, such as the Holmium's. Indeed, we chose to use the Holmium (Ho) as deposited material since this element is known to have the highest atomic magnetic moment in nature. The Holmium belongs to the lanthanide rare earths group, whose magnetic properties are substantially different form the transition metals ones, such as Iron. Rare earths have an electronic structure $5d$ $4f$ $6s$ where the exact distribution of electrons in the shells varies along the group. These systems have, for the most part, a strong paramagnetic behavior given by the highly localized moments of the $4f$ shell; below their Curie temperature they show a ferromagnetic ordering, which is the result of an interplay between the $4f$ shell and the $5d$ conduction electrons that carry an induced magnetic moment. As a consequence of the strong localized character of the $4f$ electrons, when deposited on substrates, they show stronger magnetic anisotropies as well as longer lifetimes of the magnetic states, compared to the transition metals. Out of this group of materials Holmium is the one with the highest magnetic moment, about 10.6 μ_B, and an electronic configuration $[Xe]4f^{11}6s^2$. Its crystal structure is hexagonal close packed with a lattice constant $a = 3.58$ Å, and a lattice plane distance $c = 5.37$ Å. Holmium is paramagnetic at ambient conditions, and ferromagnetic at temperatures below 19 K[2]. Soft X-ray studies combined with theoretical calculation proved that Holmium films show an antiferromagnetic helical ordering along his hexagonal axis. This behavior appears for film thicker than 10 monolayers (ML), which is well beyond the amount we deposited [32][33]. In particular, we decided to grow nanoislands of Holmium on the Ir(111) and on the Platinum (111) surfaces to study their magnetic properties; a previous STM based study involving the thermal fluctuation of iron nanoislands on tungsten was our inspiration model. Such a study involved the characterization of the lifetimes of the islands' magnetic states with regard to the environment temperature, the nanoislands' size, the tunneling current and the voltage applied to the islands, since, as explained above, the stability of such nanoislands as potential data storage units holds a great scientific interest.

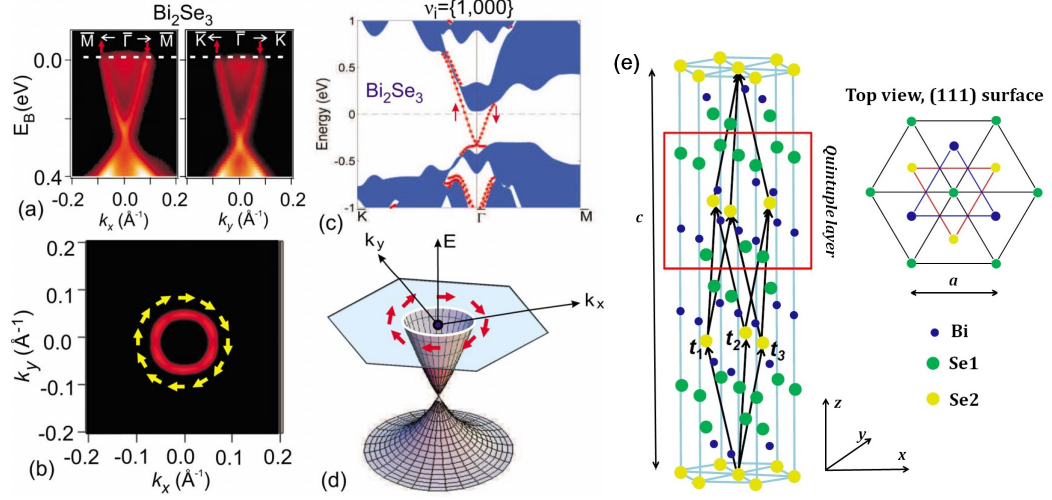[2]The Curie temperature is referred to the material in its bulk state.

Figure 1.2: (a) ARPES data for Bi_2Se_3 reveal electronic states with a single spin-polarized Dirac cone. (b) The Fermi surface exhibits a chiral left-handed spin texture. (c) computed surface electronic structure of Bi_2Se_3 (dashed line). (d) Schematic of the spin-polarized surface state dispersion. Adapted from *Hasan, Kane* [9]. (e) Crystal structure of the Bi_2Se_3. Adapted from *Zhang et al* [37].

1.3 Iron and Bismuth Selenide

The Bismuth Selenide, Bi_2Se_3, belongs to a class of material commonly known as Three Dimensional Topological Insulators (3DTI) that have drawn a lot of interest in recent years due to their peculiar properties. Among them, the so called second generation TI Bi_2Se_3 is the most used because of its plain band structure (compared to other TIs) and its phase stability - differently from other TIs the Bi_2Se_3 is not an alloy, but comes as a stoichiometric compound and, in principle, with a higher purity.

Bi_2Se_3 has a rhombohedral crystal structure, defined by its three vectors t_1 t_2 t_3, with five atoms in unit cell; commonly the crystal structure is visualized by a hexagonal cell depicted in the figure. Its lattice parameter are $a = 0.414$ nm and $c = 2.684$ nm, which equals a height of 0.955 nm for a quintuple layer. The individual layers stacked along the [111] direction are constituted of triangular lattices of only one kind of atoms. Five layers combined in the sequence Se1-Bi-Se2-Bi-Se1 form the so called quintuple layer. The atoms belonging neighboring layers of the same quintuple layer

bind strongly thanks to a strong covalent-ionic bond between the Bi and the Se; on the opposite, two quintuple layers are coupled by much weaker van der Waals interactions, leading to the (111) surface as the natural cleaving plane. The 3D Topological Insulators are insulators as the name suggests, having a band gap in the bulk, but they also show metallic states on the surface that originates from the bulk properties. The band structure for the Bi_2Se_3 is of even greater interest since presents surface states with a Dirac-like dispersion $E = \hbar v_F k_\parallel$ in the proximity of the Γ point in the Brillouin zone. This states show a very high polarization (nearly 100%) in spin, and an even more surprising coupling of the spin and the momentum k; such coupling, that goes under the name of *spin-momentum locking* locks the spin in a direction always parallel to the surface and perpendicular to the momentum [9]. Thanks to such properties, Bi_2Se_3 has a great technological interest: the spin-momentum locking forbids backscattering events and thus makes the material very insensitive to disordered surfaces with lots of defects, as long as their nature is non magnetic. As a consequence, devices with very low power dissipation and strong spin polarized current can be realized. The Dirac-like dispersion is also very versatile since by means of doping the TI or gating the device (i.e. applying a suitable bias voltage) is possible to select the current carrier density. In addition, Bi_2Se_3 has an energy gap between the valence and the conduction band of about 0.3 eV which makes it very stable even at room temperature.

On the other hand another recent discovery has drawn our interest, namely the layered iron-based superconductors. Such superconductors have shown a relatively high transition temperature Tc which widely varies depending on the specific composition of the material, and among them we have focused on the FeSe. The Iron Selenide has the simplest structure (depicted in Figure 1.4) out of all the iron based superconductors, and is far less toxic. It has found to have a critical temperature $Tc = 8K$, which can be taken up to 27K by applying an hydrostatic pressure of 1.48 GPa [19]. Over the past few years the FeSe and its properties have been extensively studied [14], but almost always in its polycrystalline form. In this project I tried to obtain a FeSe thin film with a simpler MBE procedure and to combine it with the previously introduced Bismuth Selenide. Evidence of a somewhat similar MBE growth of the FeSe under UHV condition can be found in [25]. I deposited iron particles on the Bi_2Se_3 substrate surface expecting the formation of a FeSe surface layer due to a combination of the Iron with the topmost Selenium layer in the Bi_2Se_3; the results will be presented in chapter 4.

1.4 STM studies of magnetic islands and superconductive thin films

Platinum (111) and Iridium (111) surfaces have been studied extensively with STM-STS techniques since they are widely used as substrates in combination with many materials; for this reason, a vast literature is available on this matter. Atomic resolution topographies and spectroscopic measurements can be performed as shown in BUSSE *et al.* [3], WAN*et al.* [31], Wu *et al.* [35], HOHAGE *et al.* [12]. Particularly interesting the aforementioned study of holmium single atoms on a platinum substrate[21]. The Holmium growth has been investigated on Tungsten (110) by PIASZENSKI *et al.* [16], finding the formation of triangular islands only from the second layer onward (Stranski-Krastanov mode). Finally a spin polarized STM study of Iron nanoislands on Tungsten, and its recorded telegraphic signal, are shown in Figure 1.3. The islands grow directly on the substrate surface and consist of approximately 100-150 atoms each. The telegraphic signal records the switching of the magnetic states of the islands as a function of time.

Bi_2Se_3 and FeSe have already been separately studied in the past years

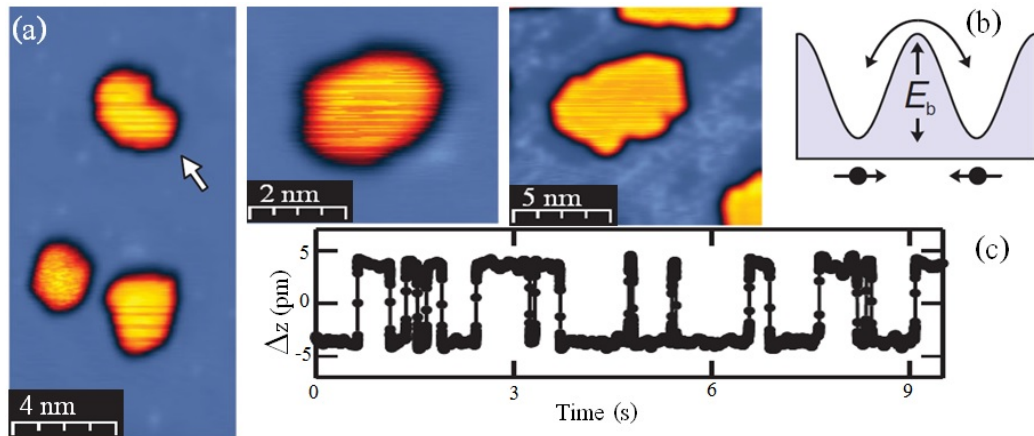Figure 1.3: (a) Spin Polarized STM topographies of nanoislads (Fe/W(110)). (b) Energetic scheme of the transition between two magnetic states. (c) Telegraphic signal observed when the tip is positioned above the island marked in (a). Adapted from *Sonntag et al* [26].

with different experimental techniques, and among these even with the STM. SONG for example directly performed microscopy and spectroscopy of a FeSe
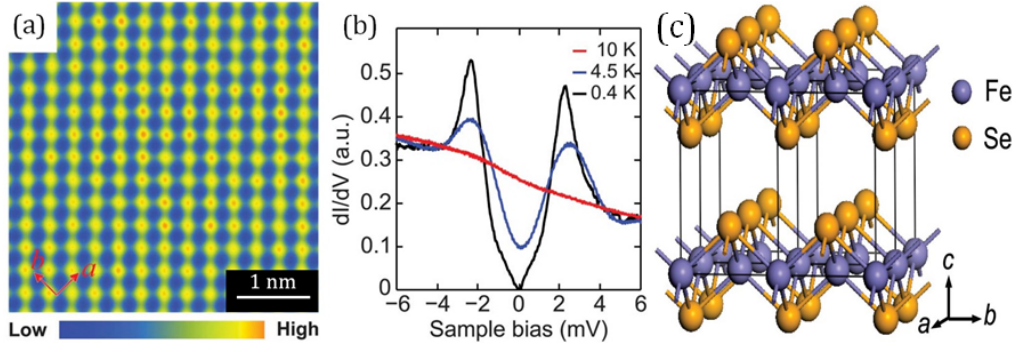
Figure 1.4: FeSe thin film on top of SiC(0001). (a) STM topography image; the bright spots corresponds to the selenium atoms in the top layer. a and b correspond to either of Fe-Fe bond directions. The spacing between two Se atoms is 3.8 Å. (b) Superconductive gap and temperature dependence of the differential conductance spectra. Adapted from *Song et al.* [25]. (c) Schematic of the FeSe structure [14].

single-crystalline thin film epitaxially grown on a SiC(0001) substrate in UHV condition [25]. He presented a topography of the rectangular lattice of the FeSe, and the spectroscopy showed a v-shaped gap up to 8 K of about 6 meV width. Bi_2Se_3 has been studied more extensively, in its pristine form by KIM *et al.* [17] for example, or even with magnetic deposited material on top - EELBO *et al.* [6], LÖPTIEN*et al.* [20] , YE *et al.* [36], and so on. Particularly interesting is the deposition of Iron single atoms performed by HONOLKA *et al.* [13], which we also used as a reference for the calibration of our Iron evaporator. A similar experiment by SCHLENK *et al.* [24] showed also how the Iron, when deposited at very low coverages (e.g. single atoms), diffuses inside the bulk of the Bismuth Selenide already at room temperature.

Chapter 2

Scanning tunneling microscopy

This chapter presents the basic principle and realization of the scanning tunneling microscopy, also explaining its benefits in developing the scientific knowledge. First, how the STM works is described outlining the experimental realization of data acquisition. Then, the scanning modes used during this work are explained. Last, the theoretical background of this method is unfolded starting from the definition of the tunnel effect and following with its theoretical models. A more detailed treatment of the theoretical approach can be found in the literature [5][34].

2.1   The microscope

Scanning tunneling microscopy and spectroscopy enable investigations on structural and electronic properties of conducting surfaces with atomic resolution. A scanning tunneling microscope (STM) consists of a sharp metallic tip which is brought in close vicinity to a conductive sample surface, such that the wave functions of the two overlap. A bias voltage U (in the range of mV to V) applied to the sample leads to a tunneling current I (on the order of pA to nA) due to the quantum mechanical tunneling effect that will be explained in more detail in the next paragraph. In the case of the STM, the insulating barrier the electrons tunnel through is ideally represented by the vacuum layer between the tip and the sample, which, on the other hand, can be seen as the two electrodes. Usual distances between tip and sample (i.e. the width of the insulating barrier) are about 5 to 10 Å. As will be shown in the following, the tunneling current has an exponential dependence

on the width of the barrier, so that even a decrease of one Å in the width results in a rise of the current of about one order of magnitude. This ensures a striking vertical resolution of the recorded signal that can be used to investigate the morphology of the surfaces down to the atomic limit. The approach between tip and sample has to be extremely well controlled in order to avoid mechanical contact and to take the most of the advantage out of this signal resolution. The movement of one electrode with respect to the other is realized by mounting one electrode on a piezoelectric device. At the state of the art, a tip mounted on a tube scanner is the most compact device for this application. When applying a voltage U_z to the z-electrode inside the scanner, the piezoelectric material, and thus the whole tube, elongates or contracts depending on the polarity. This way, the fine adjustment of the distance between tip and sample is achieved. To investigate the sample surface with lateral resolution the tube scanner can also be bent in the x and y direction in a fashion similar to the one presented above. Two couples of electrodes are fixed to the scanner, and, by applying appropriate bias voltages U_x, U_y to the electrodes, the tip can be positioned towards the sample with lateral precision. A problem on his own is instead the approach of the tip to the sample from macroscopic distances (mm). As a matter of fact, the piezoelectric material inside the scanner that is responsible for the fine adjustment along z has a range of roughly half a μm, which is clearly not enough. To solve this problem additional piezoelectric stacks are added to perform the so called *coarse approach*. In this frame, the tube scanner is inserted in a sapphire prism which is clamped by several piezoelectric stacks. The stacks move the prism stepwise by making use of friction in a slip-stick mode, being piloted by a voltage U_{coarse}. The U_{coarse} signal has the shape of a sawtooth; when ramping the voltage slowly, the prism follows the shear motion of the stacks due to friction. Conversely, when a rapid voltage pulse is applied to them they shear, and due to the inertia they slide their clamp on the prism. This approaching process is carried on until a set point for the tunneling current is reached (i.e. when a certain tip-sample distance is reached).

During STM operation, the tunneling current is recorded by a preamplifier and used as a input to the feedback loop that regulates the vertical position z of the tip. This way, the tip can scan in the x-y plane across the sample surface, and the z values are recorded at each point (x, y) of the scanning area resulting in a real-space map of the surface topography $z(x, y)$. In order to let the tip move in a line-by-line fashion, a periodic sawtooth voltage and
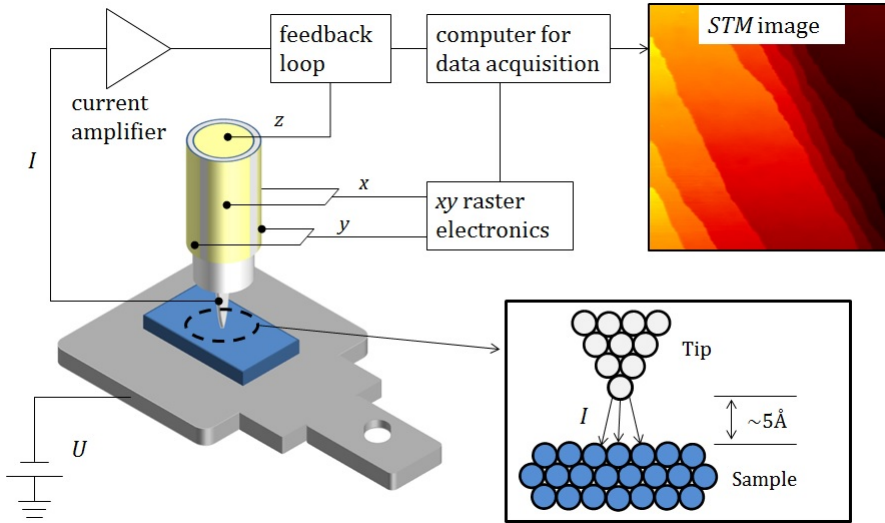
Figure 2.1: Principle of an STM. The tip, mounted on a tube scanner, and the sample are separated by a vacuum barrier of several Å. The scanner is moved applying bias voltages to its piezoelectric materials (x, y, and z). When a voltage U is applied to the sample, a current I starts to flow. The current is fed to a circuit that regulates the tip position with a feedback loop.

a slope voltage is applied to the x- and y- electrode, respectively. A calibration allows the translation of the voltage values into real height and lateral displacement. The Figure 2.1 shows a schematic view of the scanning process. The next two paragraphs present a quick overview of the measurement modes available with the STM, with particular regard to the ones that have been used during my experimental work.

2.1.1 Constant current STM

The most part of the topographies in this thesis are recorded in the *constant current mode*. In this most common mode a bias voltage U is applied to the sample and a current set point I is chosen. Then, the tip scans the sample surface line by line, and the current is kept constant with the feedback loop by using the exponential dependence of the tunneling current on the tip-sample separation. During the scanning, the feedback loop retracts the tip from the surface when the current is higher than the set point, and extends it towards the surface when the current is below the set point. The height

of the tip is recorded at every point of the scanning area. Therefore, if the sample surface is electronically, chemically and magnetically homogeneous, the tip follows the contour of the topography of the sample. To achieve the best imaging of the sample's surface one has also to pay particular attention choosing the set point for the tunnel current and bias voltage. Depending on the particular scanning situation (tip and sample natures, scanning condition *etc.*) different choices are the most suitable.

2.1.2   Constant height STM

A second scanning mode in a line by line fashion is the constant height mode. In this case the feedback loop that readjusts the height of the tip is switched off, and the tip is left at a fix z height over the sample. In contrast to the former mode, the signal is not represented anymore by the height of the tip, but by the tunneling current, which is recorded for each (x, y) position. Due to the constant height position of the tip, this mode is best to be used on flat areas of the sample; this is partially to avoid undesirable contacts between tip and sample, and partially because the measured current (that decreases exponentially with the distance) from nether areas would be too low. Under this restriction, this measurement mode is faster, since it is not limited by the feedback loop, and more insensitive to the noise. In this thesis (where specified), quasi constant height mode measurements have been performed on flat areas; this denomination refers to current signal measurements acquired at very fast scanning speed, so that even if the feedback loop is active is too slow to follow the scanning.

2.1.3   Single point spectroscopy

In this operational mode the tip is stabilized over a point of interest on the sample surface with a bias voltage U and a tunneling current set point I, which determine the tip-sample separation along z during the measurement. Then, the feedback loop is switched off with the tip kept at the stabilization position, and the current and dI/dU are recorded while the bias voltage is swept in a given range. To improve the signal to noise ratio, the $dI/dU(U)$ is measured by means of a lock-in technique. A small *ac* modulation voltage U_{mod} is added to the bias voltage and the tunneling current signal is fed to a lock-in amplifier. In my work I have used a modulation of 5 mV and a modulation frequency slightly greater than 5 kHz.
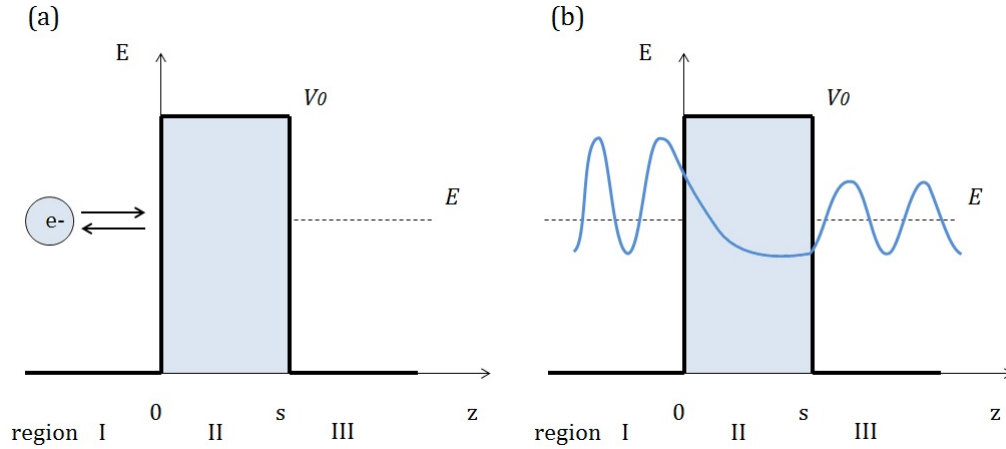
Figure 2.2: Tunnel effect in 1D. (a) in classical mechanics an electron of energy $E < V_0$ is reflected by a potential barrier. (b) in quantum mechanics the probability of the electron to traverse the potential barrier is non-zero.

2.2 The tunnel effect

The basic principle of the STM lays in the quantum tunneling of electron through a potential barrier of finite height and width. In classical mechanics a particle of energy E can overcome a potential barrier of height $V_0 < E$, otherwise it is reflected back. However, small particles like electrons have to be treated in terms of the quantum mechanics, where there is a non zero probability to cross the barrier even when $E < V_0$. This behavior can be easily shown in a sketch for the monodimensional case; we consider an electron of energy E and mass m, and a rectangular potential barrier of height V_0 and width s. Three different regions can be identified, as shown in the Figure 2.2:

region I: $z < 0$ in front of the barrier
region II: $0 < z < s$ inside the barrier
region III: $s < z$ past the barrier

In each region the electron is described by the time-independent Schrödinger equation

$$\left(-\frac{\hbar}{2m}\frac{d^2}{dz^2} + V(z)\right)\psi(z) = E\psi(z) \tag{2.1}$$

where $\hbar$ is the Planck constant divided by 2π and ψ is the electron wave function. The solutions of the wave functions in the three regions are given respectively by:

$$\psi_1 = A_1 e^{(-ik_1 z)} + A_2 e^{(ik_1 z)} \tag{2.2}$$

$$\psi_2 = B_1 e^{(-\kappa z)} + B_2 e^{(\kappa z)} \tag{2.3}$$

$$\psi_3 = C e^{(ik_2 z)} \tag{2.4}$$

where

$$k = k_1 = k_2 = \sqrt{\frac{2mE}{\hbar^2}} \quad \text{and} \quad \kappa = \sqrt{\frac{2m(v_0 - E)}{\hbar^2}}. \tag{2.5}$$

The transmission coefficient for such a system is obtained by matching the different wave functions $\psi(z)$ and their derivatives $d\psi(z)/dz$ at the discontinuity points of the potential $z = 0$ and $z = s$. This result in a transmission coefficient

$$T = \frac{|C|^2}{|A_1|^2} = \frac{1}{1 + [(k^2 + \kappa^2)^2/(4k^2\kappa^2)\sinh(\kappa s)]} \tag{2.6}$$

which can be simplified to

$$T \approx \frac{16k^2\kappa^2}{(k^2 + \kappa^2)^2} e^{(-2\kappa s)} \tag{2.7}$$

for the case of a strongly attenuating barrier ($\kappa s \gg 1$), for example if the potential barrier is too wide, or too high. This formula shows the important dependence on the barrier width; typically, $\kappa \approx 0.1$ Å^{-1}, so that a rise of the distance of 1 Å decreases the tunneling current by an order of magnitude. Although such a feature guarantees a high vertical sensitivity it has to be pointed out that the preliminary model presented here, called the wave matching method, is still not suitable to treat realistic STM experiments in three dimensions. Furthermore, particular attention was paid to the case of a single electron tunneling, whereas the STM is commonly represented by a many electrons current between two electrodes.

2.2.1 Bardeen approach

A different approach to the tunnel effect was developed by Bardeen in 1961 long before the invention of the STM. This model estimate the tunneling current from the overlap of the wave function of the two electrodes (tip and sample), using a first order perturbation theory rather than directly solving the Schrdinger equation. Bardeen assumed the electronic states of the tip and sample to be independent from each other, defining two decoupled set of eigenfunctions, eigenstates and potentials: ψ_μ, E_μ, U_μ for the sample, and χ_ν, E_ν, U_ν for the tip. He evaluated the transition probability from the state ψ_μ in the sample, to the state χ_ν in the tip. In this case, the initial state is $\Psi(0) = \psi_\mu$, and the temporal development of the total wave function is considered for positive times:

$$\Psi(t) = \psi_\mu e^{-i\frac{E_\mu t}{\hbar}} + \sum_\nu c_\nu(t)\chi_\nu e^{-i\frac{E_\nu t}{\hbar}} \tag{2.8}$$

where $\Psi(t)$ solves the time-dependent Schrdinger equation

$$\left(-\frac{\hbar^2}{2m}\Delta + U_\mu + U_\nu\right)\Psi = i\hbar\frac{\partial\Psi}{\partial t} \tag{2.9}$$

The probability for an electron to pass from the state ψ_μ to the state χ_ν is given by the so called matrix element $M_{\mu\nu}$ [15]

$$M_{\mu\nu} = -\frac{\hbar^2}{2m}\int_{Interface} d\Sigma \cdot \left(\chi_\nu^* \vec{\nabla}\psi_\mu - \psi_\mu \vec{\nabla}\chi_\nu^*\right) \tag{2.10}$$

where the integral is evaluated over an arbitrary interface in the space between tip and sample. Now, in order to apply the time-dependent perturbation theory to calculate the tunneling current one has to

- multiply $|M_{\mu\nu}|$ by the mean occupation $f(E)$ of the initial state and by the probability to find an empty one $1 - f(E)$

- sum over all states on both sides of the barrier with identical energies

- subtract the inverse transition rate

- account for the externally applied bias

By considering all possible transitions, and using Fermi's Golden Rule one gets the following expression for the current:

$$I = \frac{2\pi}{\hbar}e\sum_{\mu,\nu}\{f(E_\nu)[1-f(E_\mu+eU)]-f(E_\mu+eU)[1-f(E_\nu)]\}|M_{\mu\nu}|^2\delta(E_\mu+eU-E_\nu)$$

$$(2.11)$$

Here the Dirac function express the fact that only elastic tunneling processes are being considered (energy is conserved) since the inelastic ones have a low probability. The applied bias is accounted for by replacing E_μ with $E_\mu + eU$ in the Fermi distributions.

2.2.2 Tersoff-Hamann model

Bardeen's approach has then been improved by Tersoff and Hannan to calculate the tunneling current with specific regard to the scanning tunneling microscopy. This model simplifies Bardeen's expression by making a few assumptions. First, if one assumes to be at very low temperatures the Fermi distribution $f(E)$ can be approximated to a step function. Second, under the hypothesis of a very small applied bias potential, only the states in the proximity of the Fermi energy E_F give a contribution to the tunneling. Therefore, they obtained a simplified expression for the current

$$I = \frac{2\pi e^2 U}{\hbar}\sum_{\mu,\nu}|M_{\mu\nu}|^2\delta(E_\mu - E_F)\delta(E_\nu - E_F) \qquad (2.12)$$

In order to evaluate the current, the matrix element $M_{\mu\nu}$ has to be known, and so a set of wave functions for the tip and the sample are required (as in 2.10). Building upon geometrical consideration, Tersoff and Hamann introduced a spherically symmetric wave function for the tip (essentially s-like), oriented towards the sample and with a radius R (see Figure 2.3). Instead, for the sample they chose a freely propagating wave function along the surface of the sample, and exponentially decaying along the surface normal [27][28]. Due to what said above, the result is

$$I = \frac{32\pi^3 e^2 U \phi^2 R^2 e^{2\kappa R}}{\hbar\kappa^4}\rho_t(E_F)\sum_\mu|\psi_\mu(\vec{r_0})|^2\delta(E_\mu - E_F) \qquad (2.13)$$

where $\rho_t(E_F)$ is the tip's density of states per unit volume, $\vec{r_0}$ is the center

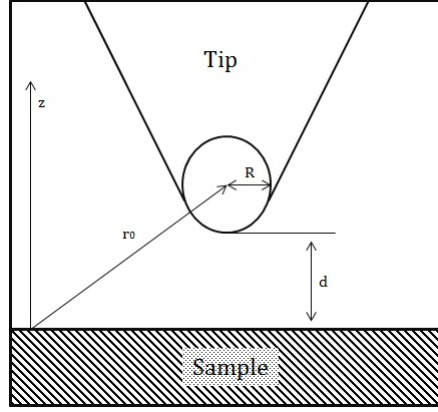Figure 2.3: Tip and sample geometry in the Tersoff-Hamann model

of the tip curvature, $\kappa = \sqrt{2m\phi}/\hbar$ is the decay rate, and ϕ is the effective barrier height which is approximately equal to the average of the tip and sample surface work functions. It is useful to note that the sum on the right equals the local density of states (LDOS) of the sample surface at E_F evaluated at $\vec{r_0}$, namely

$$\rho_s(\vec{r_0}, E_F) = \sum_\mu |\psi_\mu(\vec{r_0})|^2 \delta(E_\mu - E_F) \tag{2.14}$$

Therefore, we can write a simpler expression

$$I \propto U \rho_t(E_F) \rho_s(\vec{r_0}, E_F) e^{2\kappa R} \tag{2.15}$$

This demonstrates that topographies obtained at low bias voltage in the constant current mode represents the surfaces of constant sample LDOS at E_F measured at the center of the tip curvature at low temperature. Now, the wave function of the sample decays exponentially with distance outside the sample, i.e. $\psi_\mu \propto exp(-\kappa(R+d))$. Assuming for simplicity a constant density of states for the tip, the exponential dependence of the tunneling current on the separation between tip and sample becomes explicit:

$$I \propto e^{-2\kappa d}. \tag{2.16}$$

At finite bias, instead, equation (2.11) cannot turn into (2.12) and the basically ohmic behavior of the current with respect to the bias, no longer holds true. Generalizing equation (2.13), the current can be expressed as a

weighted convolution of the tip and sample density of states over a range of energies

$$I \propto \int_0^{eU} \rho_s(\epsilon, \vec{r_0})\rho_t(\epsilon - eU)d\epsilon \tag{2.17}$$

Referring now all energies to the Fermi level, i.e. $E_F = 0$, we apply the WKB [1] approximation:

$$\rho_s(E, \vec{r_0}) \propto \rho_s(E, x, y) \cdot exp\left(-2z\sqrt{\frac{2m}{\hbar^2}\left(\frac{\phi_t + \phi_s}{2} + \frac{eU}{2} - \left(E - \frac{\hbar^2 k_\parallel^2}{2m}\right)\right)}\right). \tag{2.18}$$

Here $z = R + d$ is the distance between the tip center and the sample, and x and y are the position of the tip on the sample surface. The exponential part in the above equation can be seen as a transmission coefficient T which depends on the energy, on the bias voltage and on the distance z. The tunneling current, therefore, results

$$I \propto \int_0^{eU} \rho_t(\epsilon - eU)\rho_s(\epsilon, x, y)T(\epsilon, eU, z)d\epsilon. \tag{2.19}$$

Particular attention has to be paid to the argument of the exponential in the equation (2.18). For any given energy E and z, a rise in $k_\parallel$ results in an exponential decrease of the transmission coefficient T. Thus, the main contribution to the tunneling current originate from the states near to the Γ point in the reciprocal space, i.e. with small $k_\parallel$. This way, T effectively favors wave vectors that are perpendicular to the surface of the sample.
Another important result here, is that by varying the applied bias, the states contributing to the tunnel current can be selected. By this principle, one can probe the local electronic density of states experimentally. Deriving the previous equation we obtain:

$$\frac{dI}{dU}(U, x, y) \propto \rho_s(eU, x, y) \cdot T(eU, eU, z) \cdot \rho_s(E_F)$$
$$+ \int_0^{eU} \rho_T(\epsilon - eU)\rho_s(\epsilon, x, y)\frac{d}{dU}T(\epsilon, eU, z)d\epsilon$$
$$+ \int_0^{eU} \left[\frac{d}{dU}\rho_t(\epsilon - eU)\right]\rho_s(\epsilon, x, y)T(\epsilon, eU, z)d\epsilon \tag{2.20}$$
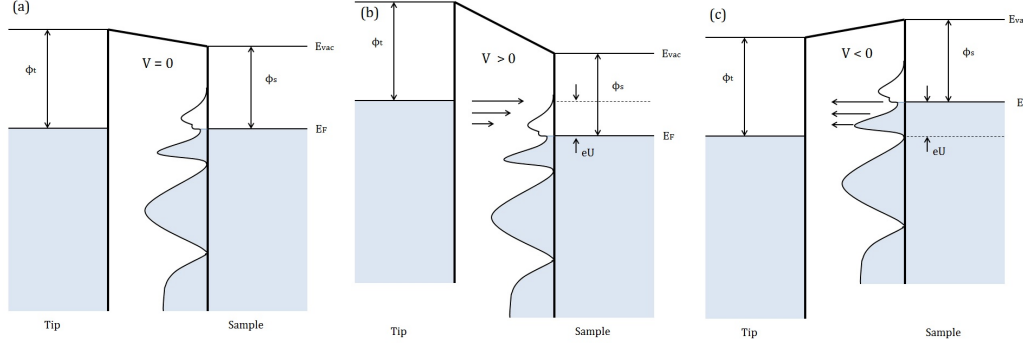
---

[1] Wenzel, Kramers and Brillouin

Figure 2.4: Electronic states involved in the STM. Filled states below E_F are indicated by shaded regions. The tip is assumed to have a flat density of states, while the sample exhibits features in the LDOS sketched by the curves. The applied voltage shifts the tip and sample Fermi level respectively. (a) equilibrium, no net current. (b) positive sample bias, net tunnel current from the tip to the sample. (c) negative sample bias, net current from the sample to the tip. The differently sized arrows indicate the decaying tunnel probability due to the effective barrier height.

If we assume a constant (or sufficiently structureless) tip density of states and a bias voltage that is small in comparison to the work function:

$$\frac{d}{dU}\rho_t(\epsilon - eU) \approx 0, \qquad \frac{d}{dU}T(\epsilon, eU, z) \approx 0$$

we can simplify the equation (2.20) to

$$\frac{dI}{dU} \approx \rho_s(eU, x, y) \cdot T(eU, eU, z).$$

This tells us that we can obtain the approximate local density of states of the sample by measuring the differential conductance. In realistic experiments the differential conductance is recorded at nonzero temperature by means of a lock-in technique with a modulation voltage U_{mod} superposed to the bias voltage U. Another angle that is worth to point out is that the transmission coefficient depends on the energetic difference to the Fermi energy. Electrons at the Fermi energy of the source electrode experience a lower effective barrier than those which lie at lower energies, as depicted in the Figure 2.4. The states close to the Fermi energy will therefore contribute stronger to the tunnel current.

2.2.3 Energy resolution

Both the theoretical models just presented assume $k_B T \ll eU$. However, at very small voltages and finite temperature, the Fermi functions of the two electrodes suffer an observable thermal smearing, effectively limiting the energy resolution. Assuming constant both the tip density of states and the transmission coefficient, the thermal broadening, and thus the thermal limitation for the energy resolution, can be estimated by [30] $\Delta E_{therm} \approx 3k_B T$. The linear dependence of the thermal energy resolution demonstrates that low temperatures are required in order to optimize the energy resolution. An additional contribution is provided by the modulation voltage U_{mod} when the differential conductance is measured. In facts, the averaging over voltages close to the bias voltage leads to an additional smearing of the experimental $dI/dU(U)$. It can be shown [10] that in this case the overall energy resolution is a combination of both thermal and modulation related limitations:

$$\Delta E = \sqrt{(\Delta E_{therm})^2 + (\Delta E_{mod})^2} = \sqrt{(3k_B T)^2 + (2.5 eU_{mod})^2} \qquad (2.21)$$

This chapter introduced the fundamentals of STM functioning and the underlying theory, without any reference to the operating conditions; in facts, such a technique has the potential to obtain information under several working environment. In the next chapter, the experimental condition of this thesis will be presented.

Chapter 3

Experimental setup

Scanning tunneling microscopy is a very powerful technique capable to perform investigation on the atomic scale and to provide information both on the morphology and on the electronic structure of surfaces. In addition, even greater results are achievable under ultra high vacuum conditions (UHV) and at low temperature: indeed, while the first ensures the absence of contamination and oxidation of the sample due to air exposure, the second improves the energy resolution of this technique.

In this chapter the instrumental setup of the UHV system is described, followed by the description of the scanning tunneling microscope and evaporators utilized during my work; furthermore, a brief explanation about the evaporators calibration, and the preparation of the tips is inserted.

3.1   The UHV system

All the experiments have been performed in the ultra high vacuum system shown in Figure 3.1. As shown in the figure, the system consists of two chambers, the preparation and the analysis chamber. In addition, a four slots fast-entry lock is attached to the preparation chamber, so that samples and tips can be introduced into the system without breaking the vacuum regime. The two chambers and the fast-entry lock are connected by different valves which can be shut to achieve different pressures when needed. Indeed, while the preparation chamber is normally used to clean the samples, the analysis chamber holds the STM and it is where the measurements are performed. For this reason, the two chambers have generally different base
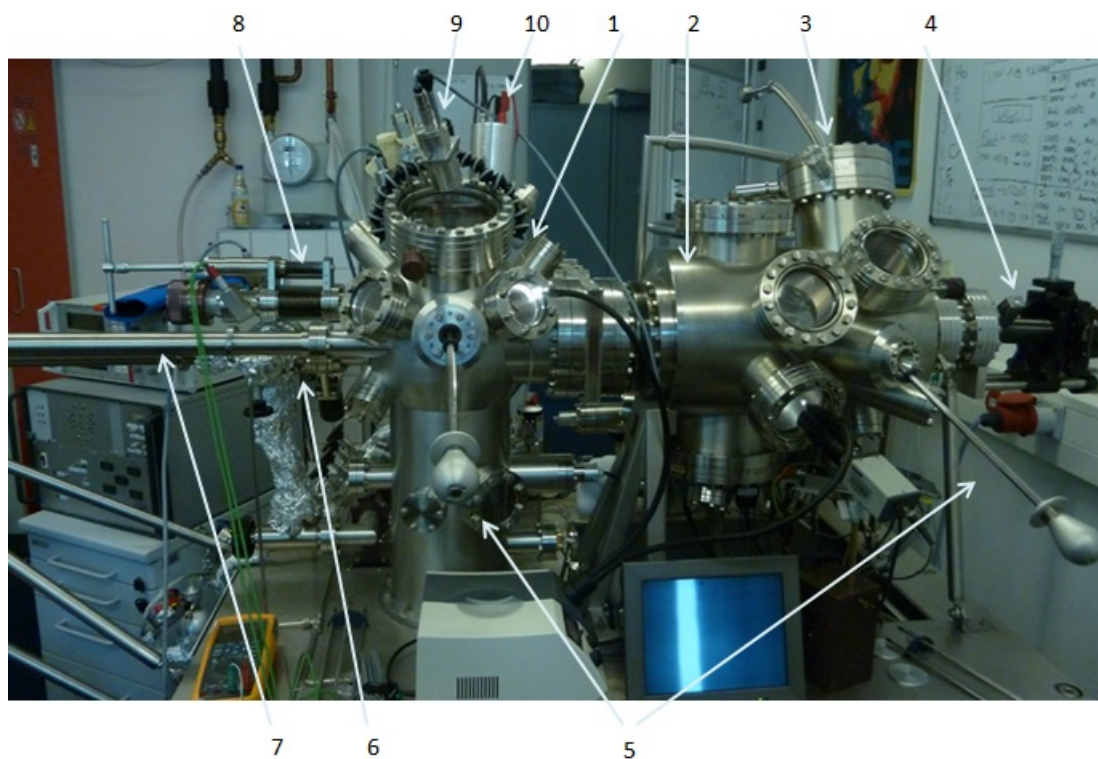
Figure 3.1: Photograph of the UHV system. (1) Preparation chamber (2) analysis chamber, (3) LEED & Auger appliances, (4) cold manipulator, , (5) wobble sticks, (6) fast-entry lock(7) transportation arm, (8)Manipulator for the sputtering, (9) pyrometer, (10) electron beam cannon.

pressures: 10^{-9},10^{-10}mbar in the preparation chamber, and 5×10^{-12}mbar in the analysis chamber. The fast-entry lock, instead, is usually at ambient pressure and is pumped to the pressure of the preparation chamber only when needed. The vacuum is achieved thanks to a turbopump, a ion pump and titanium sublimation pumps (tsp) in the preparation chamber, and a ion pump and tsp in the analysis one. The preparation chamber is equipped with a sputter gun and an electron beam heater to clean the sample; in addition a removable mass spectrometer is available. Also, there is a line that connects small gaseous cylinders (usually Argon and Oxygen) and the chamber; this line is used either to sputter the samples, or to oxidate the samples (useful for the oxygen annealing) or to perform Chemical Vapor Deposition (CVD) on them (e.g. with Ethene dewars). The sputter gun can provide a maximum sputter current of $1.3\mu A$, and the electron beam heater can heat a sample well beyond 2000 °C. The temperature is checked by means of an infrared pyrometer, whose lowest temperature reading is 249 °C. Furthermore, there is a second resistive manipulator heater, which can be monitored with a thermocouple. The analysis chamber harbors the STM and a twenty slots carousel which is used to store multiple tips and samples under vacuum conditions. Moreover, the analysis chamber is equipped with six evaporators that contain each different materials to be deposited either on the samples or on the tips, as will be discussed in the following. Finally, inside the chamber there are a LEED and an Auger instrumentation, and a manipulator which can be used either as a heater or as a cooler (especially useful for different temperature depositions). In particular, since the manipulator is cooled with an external supply of liquid nitrogen, the lowest temperature achievable is ≈ -180 °C. The samples are mounted on tungsten sample holders and, depending on the nature of the sample, they are fasten to them thanks either to a tungsten wire, or to a special conductive glue. Finally, the samples are moved around inside the chamber with two transportation arms and two wobble sticks, attached respectively to the preparation chamber and to the analysis chamber.

3.2 The STM

The microscope that I used during my work is a variable temperature STM built by the Hamburg University research group. In this system the temperature of the sample can be varied, while the tip is always at ambient

temperature. The lowest stable working temperature is 25-30K; such a temperature is achieved thanks to a constant liquid helium cooling system (T liquid helium $\approx$4.2K). The helium is provided by an exchangeable dewar and the cooling reaches the STM through a cryostat and thin gold coated wires. The temperature of both STM body and cryostat is observed with thermocouples, and, under normal operation condition, there is a difference of 10K between them. Furthermore, the very microscope is shielded against the light radiation by a metal cover whose temperature is kept to 70K. The STM body is made of phosphor bronze and gold coated to reduce the oxidation of its surface. The samples are introduced in the STM with a wobble stick and two springs are used to clamp the sample to the body of the STM; the contact between the sample and the body ensures thermal contact as well as the grounding of the sample itself. The thermal equilibrium of the sample at 30K is reached, when inserted in the microscope, within 10 minutes. Note that in this configuration the sample is facing downwards and the tip is approaching the sample from below. In our case the tip is the moving element, an thus the tip scans along the sample. The tip is held by the tip holder which is inserted in the scanner. As explained in the previous chapter, the scanner movement is given by piezoelectric actuators. The tip approaching to the sample is manually controlled down to millimetric distances and then an automated coarse approach brings the tip at the distance of few nanometers. The coarse approach is given by six shear-piezoelectric stacks inside the body of the STM. By means of a metal leaf spring the six piezoelectric stacks clamp a sapphire prism that holds the scanner and the tip. The body of the STM can be either fixed to the UHV system or to a so called damping stage, whose purpose is indeed to reduce to a minimum the effects of mechanical vibrations that would otherwise propagate to the tip and would in the end result as noise in the data. The damping stage makes use of springs and of a system of magnets and eddy currents to get rid of the vibrations. In the Figure 3.2 below is shown a photo of the STM with its shield, and its schematic view from the front and below.
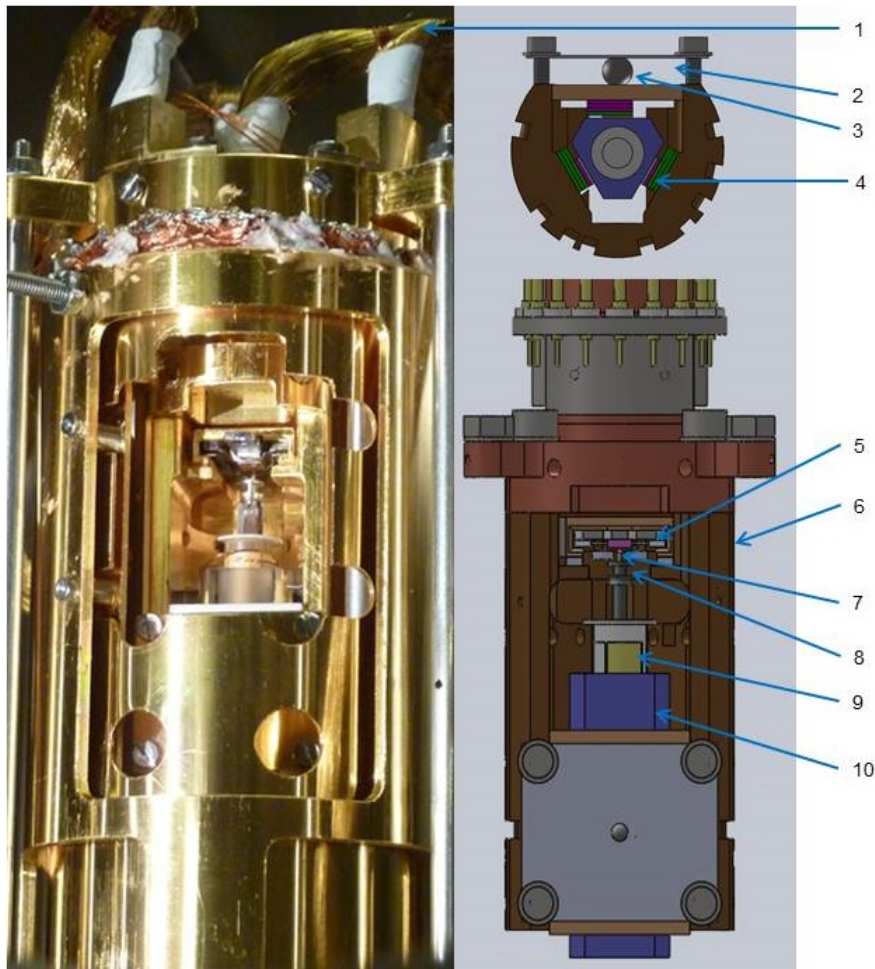
Figure 3.2: Photograph and schematic view of the STM. (1) Cold wires for the scanner cooling, (2) leaf spring, (3) stainless steel ball, (4) shear-piezo stack, (5) sample inside the sample stage, (6) gold plated STM body, (7) tip, (8) tip holder, (9) scanner piezos, (10) sapphire prism.

3.3   Evaporators

The evaporators are used to perform Molecular Beam Epitaxy (MBE). To achieve a clean (contamination free) deposition onto the samples, an evaporator has to be degassed thoroughly to get rid of every contamination, such as water, carbon oxide, and so on. As well, also the crucibles that harbor the material, and the material itself have to be degassed in a similar way. To degas the evaporators, as well as the crucibles and the materials, I transferred the evaporator in a different vacuum chamber, whose purpose is indeed to degas and calibrate evaporators, so to keep clean the original UHV systems. The base pressure of this system is around 10^{-7}mbar. For the degassing, the evaporator is run at usual operating parameters for hours inside the chamber, until the pressure stabilize to its minimum; this is to ensure that most of the contamination is removed. As said above, the procedure is repeated once with the crucible inside, and once again with the material inside too. During my work I used two different kinds of evaporators, an electron beam evaporator, and an effusion evaporator, namely a Knudsen Cell. The electron beam evaporator uses a filament and a potential grid to emit electrons that are accelerated towards the material. As a consequence of the kinetic energy of the electrons, the material melts and evaporates. Normally, such evaporators are used in combination with rod-like shaped materials for evaporation. Vice versa, the Knudsen Cell simply heats the material, which is stored as scales in a long crucible, by means of the filament, without the electron beam. While the first kind of evaporator was used for the deposition of Iron as will be presented in Chapter 6, for Holmium deposition the use of the second kind was more suitable, mainly for two reasons. Firstly, the evaporation materials come with a higher purity level when they are synthesized in scales, rather then in rods. Secondly, rare earths materials such as Holmium are easy to ionize and to form plasmas when used in combination with electron beam evaporators in a vacuum system with a pressure higher than 10^{-7}mbar.

3.3.1   Calibration of evaporators

In order to correctly deposit a material onto a substrate it is fundamental to know, at least to a reasonable degree, the amount of material evaporated; to do so, a calibration is needed. There are different methods to gauge the flux of an evaporator; in the following is explained the one I used. Given a clean surface without adsorbates on top, the evaporator is switched on for a short

Figure 3.3: Electron beam evaporator, and Effusion evaporator (Knudsen-Cell) with its crucibles, left and right respectively

time, e.g. tens of seconds. Hence, the sample is examined with the STM and a number of topography images are taken; then the number of single particles evaporated are counted over a single image. For a single image, one can estimate the evaporation rate in mono layers (ML) per second as

$$\Phi(ML/s) = \frac{\text{number of atoms evaporated}}{\rho_s A \tau}$$

where ρ_s is the surface density, i.e. the atomic sites for area unit (which depends on the particular substrate and its orientation), A is the area of the image and τ is the exposure time. At last, the Φ rate is averaged over different images for a more precise gauge. A calibration example will be shown in Chapter 4 for the case of Fe on Bi_2Se_3.

3.4 Tip preparation

During my experimental activities I have used chemically etched Tungsten tips. Farther on, is explained the procedure carried out for the tip making. This electro-chemical procedure is well known in literature as drop-off method. Firstly the tip holder has been coarsely cleaned in an ultrasonic bath of isopropanol ($CH3CH(OH)CH3$). Then, a Tungsten wire of 0.75 mm was inserted in the tip holder and fixed inside by bending it. Hence,

the wire apex and the tip holder were wrapped in a parafilm layer leaving
exposed the portion of the wire to be etched. The wire has been immersed
upside down in an aqueous solution of NaOH (the electrolyte), inside whom
a 4.5 V AC potential difference was applied between the wire and a carbon
rod counter electrode. Due to this tension, the etching begins; the etching
takes normally a couple of minutes to carve the wire, whose top in the end
falls because of its own weight, leaving an elongated tip apex. After carefully
removing the parafilm the tip was introduced in the UHV system. Finally,
the tip was degassed and flashed at 1700 °C to remove the native oxide layer
(WO_2, WO_3), and inserted in the STM.

Even though the tip is ready after this procedure, in time it deteriorates, due
to scanning on different surfaces or due to the contaminations. Therefore, a
continuous process of tip improving is necessary, by flashing again the tip,
or pulsing on clean samples (applyng greater voltage biases between tip and
sample for a very short amount of time), and other methods.

Chapter 4

Results

4.1 Introduction

This chapter presents the experimental results obtained in the time frame of this thesis. The result mainly refer to a scanning tunneling microscopy study of Holmium growth on Iridium and Platinum, and of Iron growth on Bismuth Selenide; important properties of these materials are summarized in the first chapter of this manuscript. Each growth study is treated separately, at first providing an overview of the sample preparation, and then presenting the result. Before that, however, it is necessary to explain the terminology used in this chapter, *i.e.* what is intended for clusters and islands. By our definition we refer to cluster as aggregates of atoms deposited on the surface that do not show any periodicity structure. On the opposite we refer to islands as periodic structures where a clear crystallographic direction is defined. When visualizing an island, is impossible to identify a lattice, we take as a valid clue the presence of a smooth surface on top and a well defined perimeter of the island.

4.2 Holmium on Iridium(111)

4.2.1 Iridium preparation

The pristine Iridium (111) surface has been cleaned by means of cycles of sputtering, Oxygen annealing, and flashes in the preparation chamber, in a base pressure of 10^{-9} mbar. The Carbon that resurfaces from the bulk
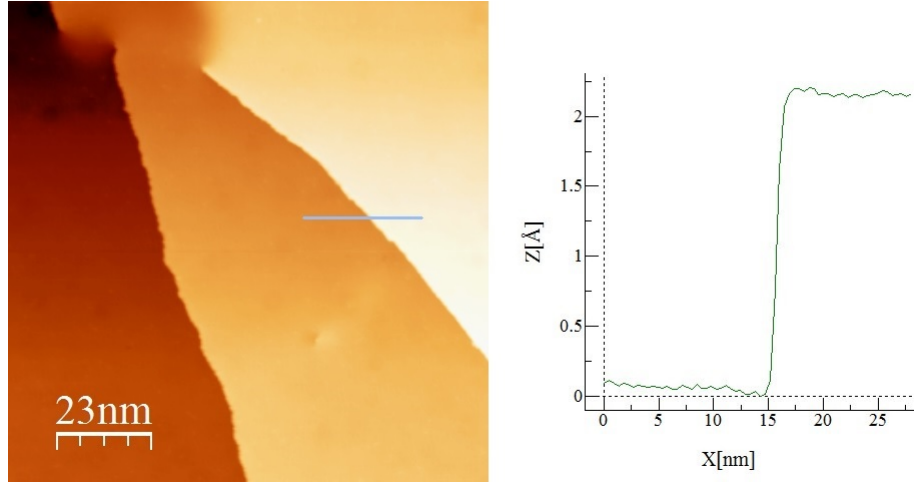
Figure 4.1: Pristine clean Iridium (111) surface. In the right panel is shown the profile of a step edge along the line in the image. The step height is 2.2 Å in accordance with the literature, which ensures a correct calibration of the scanner. Scanning parameters: $U = 80$ mV, $I = 100$ pA.

due the annealing has to be removed by covering the sample in an Oxygen atmosphere, usually between 5×10^{-6} and 5×10^{-9} mbar. Indeed, the Oxygen can bond with the Carbon forming CO, that is less fasten to the surface. Eventually, the CO is removed from the surface with a flash, i.e. by taking the sample to high a temperature for a short time, so that the CO desorbs and at the same time no more impurities can resurface. A cycle normally consisted of:

- Sputtering for one hour (3.9 μA)

- Flash at 1180 °C for 20 seconds

- Sputtering for 30 minutes (3.9 μA)

- several Oxygen Annealing cycles at 1180 °C starting at 5×10^{-7}mbar and decreasing till 10^{-8} mbar with a flash in between each of them in order to remove the CO from the surface

This procedure, which normally has a trial and error development, has been carried out many times, until the sample reached a satisfactory cleanness. An example of a clean Iridium(111) surface is shown in the Figure 4.1.
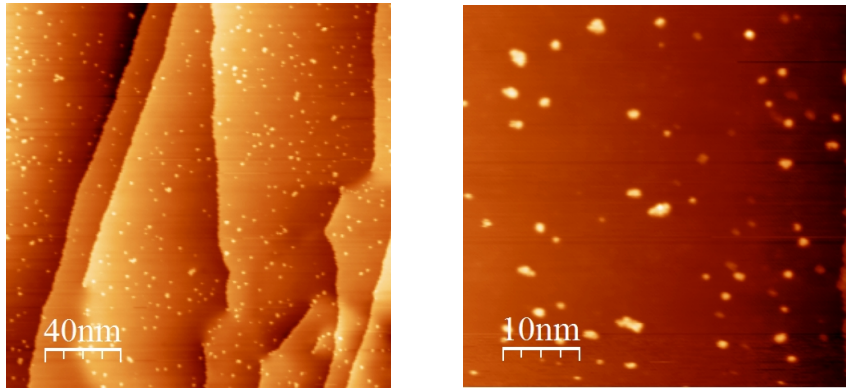
Figure 4.2: Ho on Ir(111). Deposition for 30 seconds at room temperature. Images' sizes 200×200 nm^2 and 50×50 nm^2. $I = 50$ pA, $U = 400$ mV.

Once clean, the substrate has been transported in the analysis chamber for the Holmium deposition. Every deposition has been made on the Iridium at room temperature, while the Holmium has been evaporated from scales at 850 °C with a Knudsen-Cell evaporator, described in Chapter 3.3.

4.2.2 Holmium deposition

At first, I deposited a low amount of Holmium to calibrate the evaporator, and then I kept on increasing the amount of deposited material, annealing the sample after every addition with increasing temperatures between 250 and 650 °C. The Figures from 4.2 to 4.9 show the process. Already from this very first set of depositions one can already take notice of the Holmium tendency to form no islands. On the other hand, is clear how the Holmium atoms gather to form clusters as a consequence of the thermal energy given by the annealing. Indeed, after the annealing the atoms gather to a cluster, but once one is formed, the cluster doesn't join others to form a bigger island. This suggests that there is no additional energy barrier to be exceeded by heating the sample; moreover, further increasing the temperature would possibly result in the desorption of the Holmium, or in its alloying with the substrate. It is useful to note that due to the step by step procedure we followed we can rule out the presence of a Holmium first layer in our topographies, so that only the interaction between the deposited Holmium and the substrate is shown. After this preliminary study the Iridium sample has been cleaned to start a new fresh deposition. I deposited the same
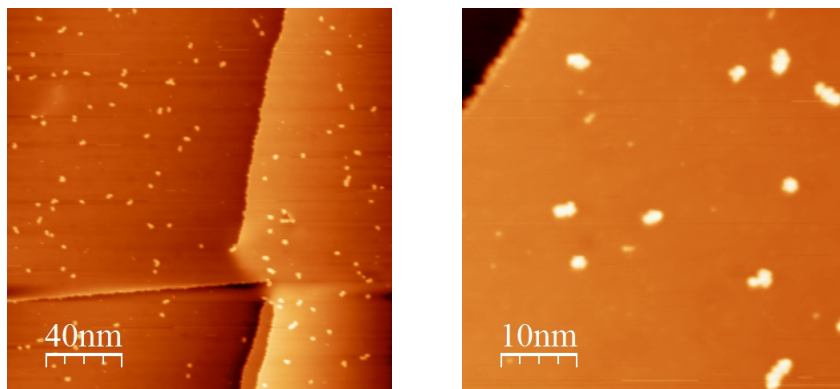
Figure 4.3: Ho on Ir(111). Annealing for 4 minutes at 250 °C. Images' sizes 200×200 nm^2 and 50×50 nm^2. $I = 50$ pA, $U = 400$ mV.
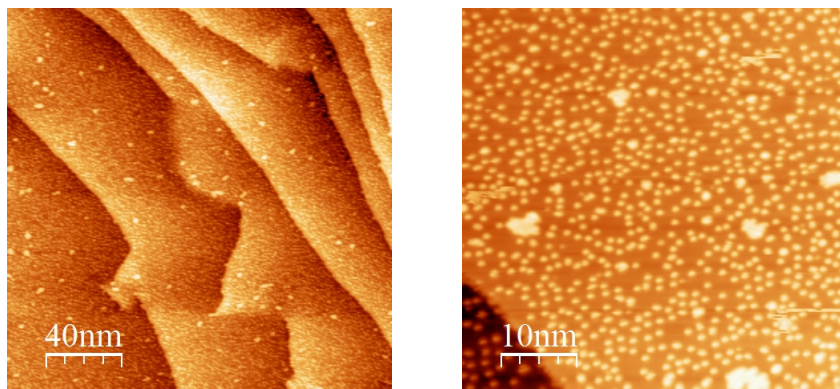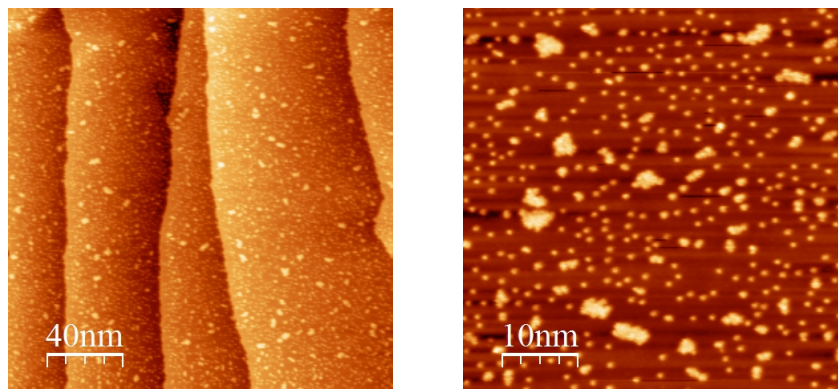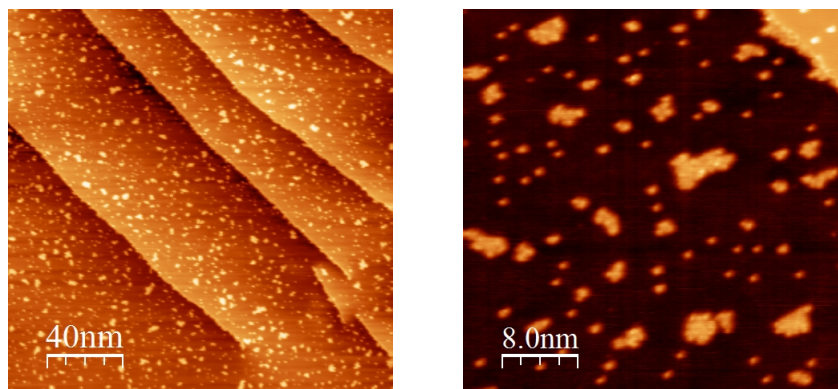

Figure 4.4: Ho on Ir(111). Additional deposition of 90 seconds at room temperature. Images' sizes 200×200 nm^2 and 50×50 nm^2. $I = 50$ pA (left), and $I = 150$ pA (right); $U = 400$ mV.

Figure 4.5: Ho on Ir(111). Annealing for 4 minutes at 250 °C. Images' sizes 200×200 nm^2 and 50×50 nm^2. $I = 50$ pA (left), and $I = 100$ pA (right); $U = 40$ mV.

Figure 4.6: Ho on Ir(111). Annealing for 6 minutes at 350 °C. Images' sizes 200×200 nm^2 and 40×40 nm^2. $I = 50$, $U = 400$ mV.
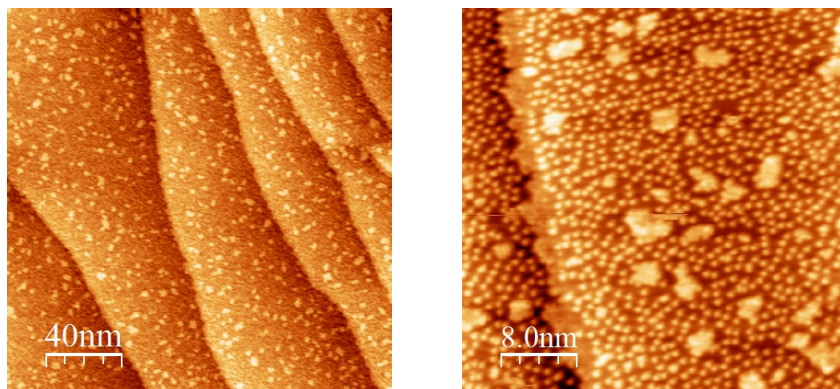
Figure 4.7: Ho on Ir (111). Additional deposition of 3 minutes at room temperature. Images' sizes 200×200 nm^2 and 40×40 nm^2. $I = 50$ pA, $U = 400$ mV.

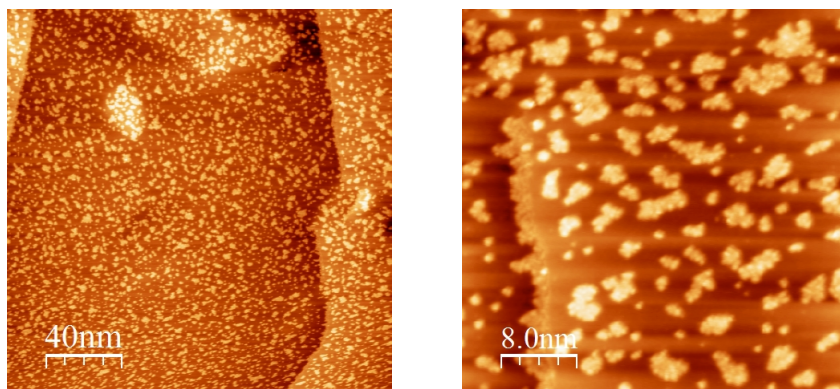Figure 4.8: Ho on Ir(111). Annealing for 6 minutes at 450 °C. Images' sizes 200×200 nm^2 and 40×40 nm^2. $I = 50$ pA, $U = 400$ mV.
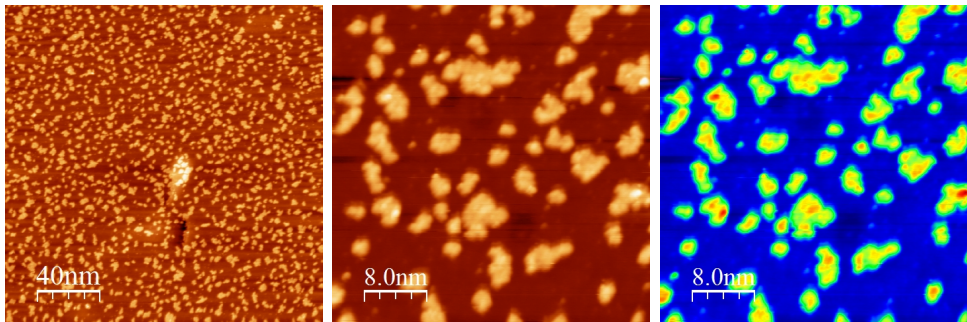
Figure 4.9: Ho on Ir(111). Annealing for 5 minutes at 550 °C. In the right panel the same image shows the roughness on the clusters by using a different color scale. Images' sizes 200×200 nm^2 and 40×40 nm^2. $I = 20$ pA, $U = 400$ mV.

total amount of the previous cycle, and then annealed the sample at 650 °C for 6 minutes. Although in this case the cluster have a size slightly bigger compared to before, especially after the annealing (Figure 4.10, right panel), there is still no evidence of island formation. The clusters have an average radius of 5 nm (rarely exceeds 10 nm), and a height of approximately 2.3 Å, very similar to the Iridium's step height. Their contours appear to be jagged as well as their surface (Figure 4.11); in particular, no evidence of a defined crystallographic direction has been found. After this second deposition, which according to our calibration should have amounted to half a monolayer, the Iridium substrate has been cleaned once again. The last deposition has been performed doubling the exposure time for the evaporation; no annealing was performed this time. Even in this case the Holmium forms no islands on the Iridium(111), but rather clusters. The cluster's size is almost the same, while just the distance among the adatoms has shrunk. It is indeed important to take notice of the behavior of the single Holmium adatoms on the surface, which is visible since the early deposition and at best in the last one: the atoms seem to repel each other and to form an exagonal superlattice on the surface, even though is still in a premature stage. This phenomenon could suggest a coulombian-like repulsion, which is characteristic of charged particles. Indeed there are several examples of deposited molecules that become charged due to interaction with the substrates [7][29]; however, at the present case we are dwelling about two metals, and so this behavior, if not fascinating, is at least puzzling. In Chapter 5, a further analysis on this
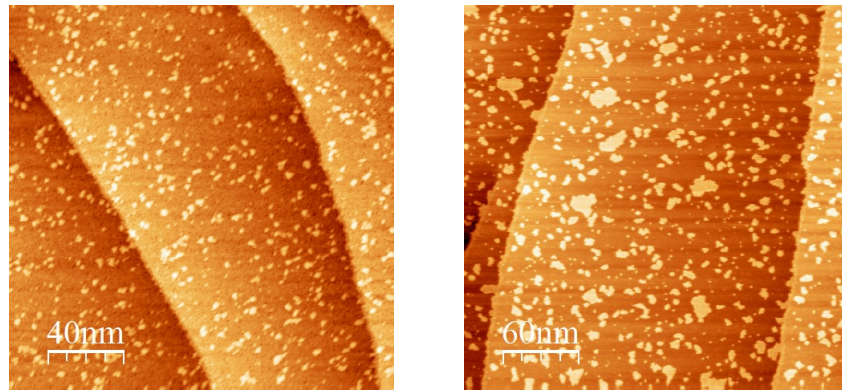
Figure 4.10: Ho on Ir(111). Deposition of 5 minutes (left panel), and annealing at 650 °C for 6 minutes (right panel). Images' sizes 200×200 nm^2 and 300×300 nm^2. $I = 50$ pA, $U = 400$ mV.
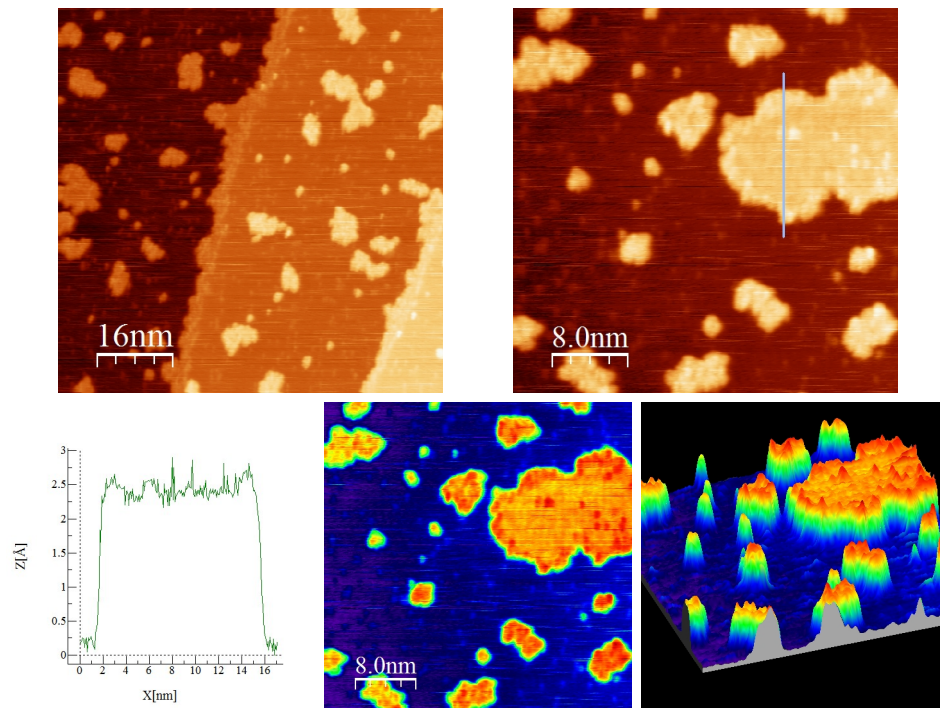

Figure 4.11: Ho on Ir(111). Close view of the clusters, and cross section along the line in the image. Different color scale images in 2D and 3D that show the indented surface of the cluster. Images' sizes 80×80 nm^2 and 40×40 nm^2. $I = 50$ pA, $U = 400$ mV.
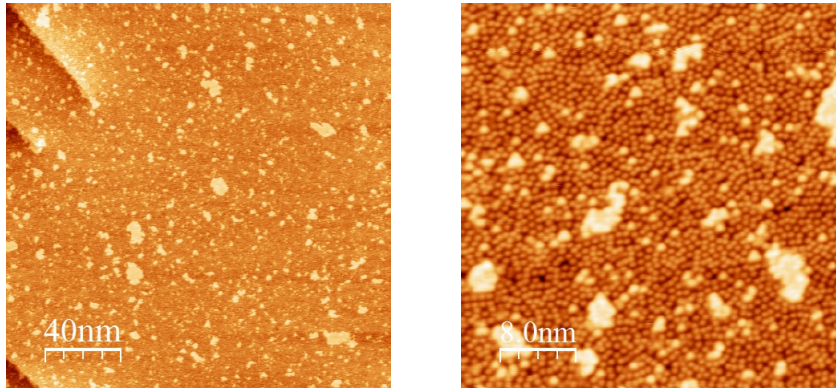
Figure 4.12: Ho on Ir(111). Deposition of 10 minutes at room temperature. Images' sizes 200×200 nm^2 and 40×40 nm^2. $I = 20$ pA, $U = 400$ mV.

matter will be presented.

4.3 Holmium on Platinum(111)

4.3.1 Platinum preparation

The Platinum crystal has been cleaned in a fashion similar to the one used for the Iridium. Due to the different melting points of the two materials, the annealing and flashing temperature have been changed: in particular, I annealed the sample at 740 °C and flashed it at 1080 °C. Figure 4.13 shows the Platinum surface before, and after the cleaning procedures.

4.3.2 Holmium deposition

To be consistent with the last deposition on Iridium, I evaporated for 10 minutes (nominally 1ML), at room temperature; no annealing has been performed on the sample. As shown in Figure 4.14, no islands are observed, but clusters, as well as scattered atoms repelling each other; hence, what obtained is indeed a similar result to the one obtained for the deposition on Iridium. The clusters occupy a larger area compared to before (about two times bigger), whereas their height remains the same; in addition they tend to elongate rather than to enlarge isotropically as in the case of the Iridium. Finally, their edges are jagged as well as their surface, due to the
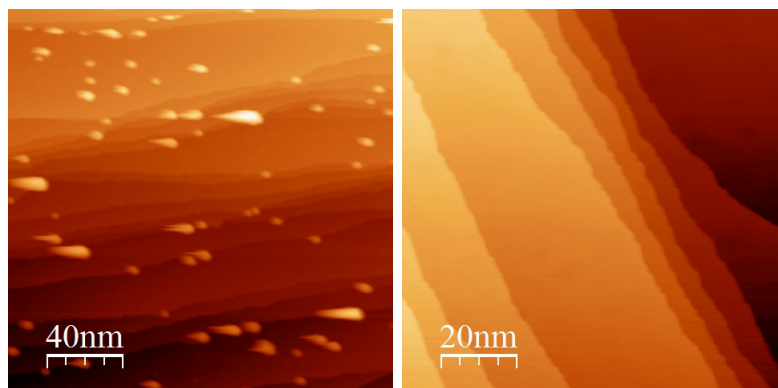
Figure 4.13: Pristine Platinum (111). The images show the Platinum surface before (left panel) and after the cleaning cycles (right panel). Images' sizes 200×200 nm^2 and 100×100 nm ^{2}. $I = 20$ pA, $U = 1$ V.

poor ordering of the atoms on top. Given the present result I forsook my initial aim to grow Holmium islands, in order to pursue a better comprehension of the alleged repulsion between the Holmium atoms on the surface. As previously observed in the former paragraph, the thermal energy causes the Holmium atoms to cluster together through the annealing; in addition, one could hypothesize that the presence of such clusters somehow perturbs the distribution of the adatoms. Thus, I tried to minimize the clusters, and possibly to obtain an ordered adatom distribution on the surface, by cold depositing the Holmium. After cleaning the Platinum crystal I performed a cold deposition at ≈ 90 K, depositing once again one nominal monolayer. As a matter of facts, the deposited atoms bond to the cold surface, which doesn't provide them the energy to travel along the lattice, and group together in clusters. By looking at the Figure 4.14 one can see that the size and number of the clusters is reduced, and the atoms are packed closer to each other. Even so, by closely looking at the distribution of the atoms, and comparing it to the Figure 4.12, the present disposition of atoms seems to be less ordered compared to the one onto the Iridium. Since the adatoms still repel each other, but order – and hence interact – differently, an active role of the substrate has to be taken into account. In the following chapter I will present an analysis about the adatom ordering with the help of a calculator.

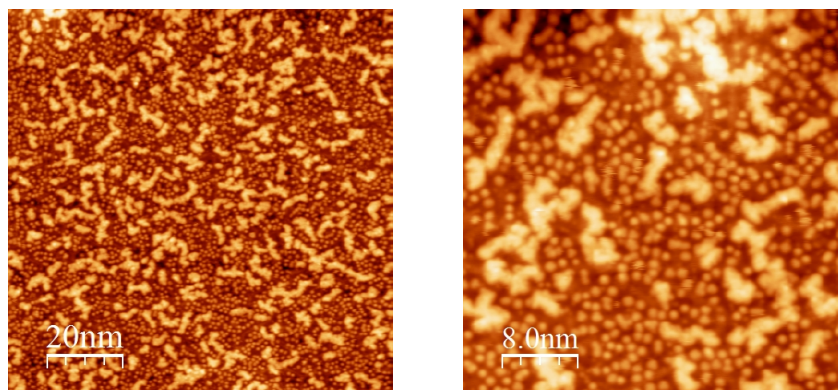Figure 4.14: Ho on Pt(111). Deposition of 10 minutes at room temperature. Images' sizes 100×100 nm^2 and 40×40 nm^2. $I = 100$ pA, $U = 1$ V (left panel), and $U = 500$ mV (right panel).
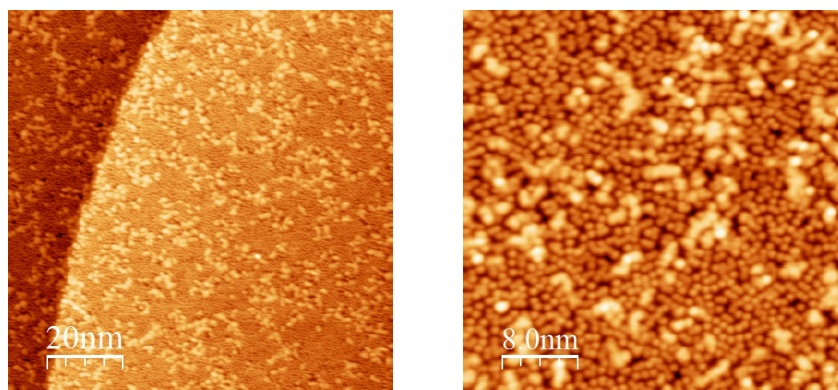

Figure 4.15: Ho on Pt(111). Cold deposition for 10 minutes at -180 °C. Images' sizes 100×100 nm^2 and 40×40 nm^2. $I = 20$ pA, $U = 1$ V (left panel), and $U = 50$ mV (right panel).

4.4   Iron on Bismuth Selenide

4.4.1   Bi$_2$Se$_3$ preparation and calibration of the evaporator

The kind of samples such as the Bi2Se3 and the other topological insulators cannot be cleaned by normal STM procedures, i.e. sputtering, annealing, oxygen annealing. On the other hand, this materials are very easy to exfoliate and to remove their topmost layers by means of a scotch tape. Getting advantage of this property, the best way to obtain a clean sample is to cleave them *in situ*. To do so, one end of the scotch tape is applied on the material surface, and the other end on a slot of the fast-entry lock in the UHV system. Then, both the sample and the tape are introduced inside the preparation chamber, where the scotch tape is removed with the wobble stick, thus cleaving the sample; this way, only a not contaminated surface remains on top of the sample. For our sample we have followed the procedure just explained. After the cleaving *in situ*, the sample has been immediately moved to the analysis chamber for the calibration of the Iron evaporator. The proceedings for the calibration of an evaporator are explained with more details in Chapter 3.3. As a reference for my calibration I also used the article [24]. The deposition of the Fe for the calibration has been carried out at low temperatures ($\approx$ the bulk of the Bi$_2$Se$_3$ is at 90 K) since the Iron atoms tend to diffuse into the bulk at higher temperatures [24] (Figure 4.14). To calibrate the evaporator a total area of 7000 nm^2 has been used, as well as a surface density $\rho_s = 6.74$ at/nm^2 for the Bi$_2$Se$_3$. Evaporating for $\tau =10$ seconds onto the sample we obtain a flux

$$\Phi(\mathrm{ML/s}) = \frac{556\mathrm{atoms}}{6.74\mathrm{at/nm^2} \cdot 7000\mathrm{nm^2} \cdot 10\mathrm{s}} \approx 0.0012\mathrm{ML/s}$$

which approximately equals a monolayer every 15 minutes. Once the calibration was done, every other deposition of Fe has been carried out at ambient temperature. At first, according to our calibration, we deposited 1ML of Fe; then, the sample has been annealed for 15 minutes at 200 °C. At this stage only clusters are visible, as shown in Figure 4.17; this is also due to the poor condition of the tip, since it is not rare to temporarily pollute it by scanning on surfaces such as the Bi$_2$Se$_3$. Hence, additional 2ML have been deposited, and the sample was annealed right afterwards once again at 200 °C for 15 minutes. Consequently, the presence of islands is observed, though not ut-
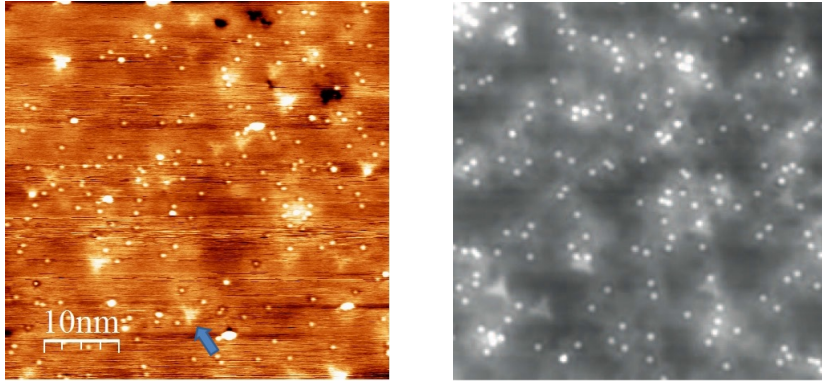
Figure 4.16: Fe atoms on Bi_2Se_3. Left panel: Iron atoms cold deposited on a pristine Bi_2Se_3, which can be distinguished thanks to the characteristic features (pointed by the arrow) due to Selenium vacancies. $I = 20$ pA, $U = 1$ V. Right panel: image adapted from Honolka *et al.* [13]. In both images the coverage is $\approx 1\%$.

terly flat. The height of the islands varies between 3.5 and 5 Å, and their average area is about 20×20 nm^2. There is also evidence of some islands growing on top of each other (bright spot in Figure 4.17). Finally, I have annealed the sample for 80 minutes, looking for further modification of the sample due to thermal energy. Such long times for the annealing are sometimes required since it is not possible to rise the temperature beyond 200-250 °C. The Bismuth Selenide is synthesized in scales that are then glued to the sample holder by means of a conducting glue, whose melting temperature is slightly above 300 °C. No major differences in the sample has been found after the annealing. However, a few things are to be said concerning the islands.

Searching the islands surface throughly, one can find a rectangular lattice on top, which is clearly in contrast with the hexagonal lattice, typical of the Bi_2Se_3. Furthermore, the measured distance between two nearest neighbors in the rectangular lattice is about 3.5 Å, while for the Bismuth Selenide is 4.14 Å [37]. The rectangular lattice has been measured in both directions through the program WSxM; the interatomic distance is evaluated by averaging it over several atoms. Two hypothesis seem to be the most likely to explain these findings. On one hand, the islands could be pure iron islands: the Iron has a Bcc structure that could show a rectangular reconstruction. However, the lattice constant is about 2.87 Å that doesn't match the measured value.
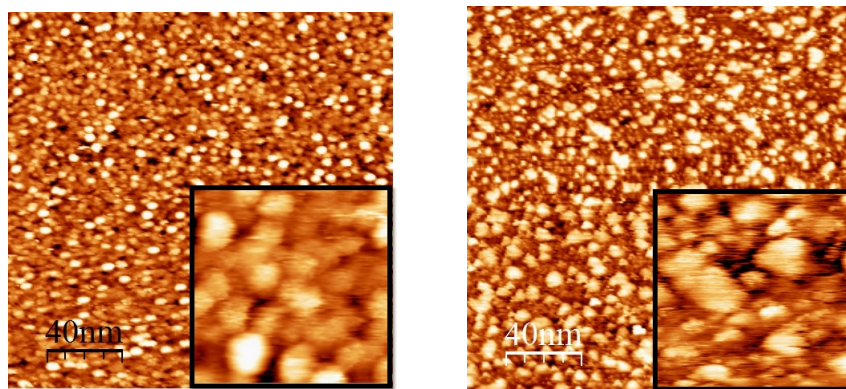
Figure 4.17: Fe on Bi$_2$Se$_3$. Left panel: after deposition of $\approx$1 ML. Right panel: after annelaling for 15 minutes at 200 °C. Images' sizes: 200 × 200 nm^2, 25 × 25 nm^2 (the insets). $I = 20$ pA, $U = 1$ V.
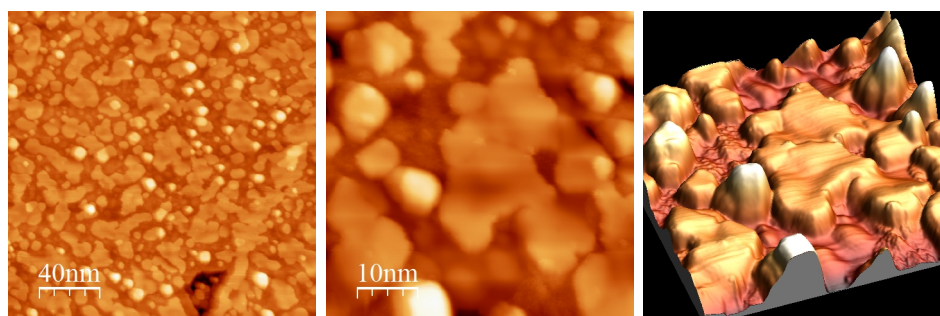

Figure 4.18:]
Fe on Bi$_2$Se$_3$. Additional deposition of 2 ML at room temperature. The 3D projection in the right panel shows the smooth surface of the islands. Images' sizes: 200 × 200 nm^2, 50 × 50 nm^2. $I = 20$ pA, $U = 1$ V.
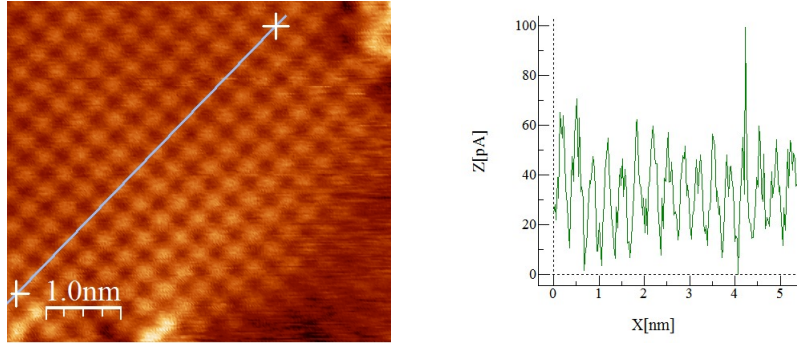
Figure 4.19: Fe on Bi_2Se_3. The image, taken in quasi-constant height mode, shows a close view on one island; the rectangular lattice is clearly visible. The graph shows the cross section along the line in the image, whose peaks correspond to the atom position. The average interatomic distance is 3.5 Å. $I = 150$ pA, $U = 0.5$ V.

A different hypothesis is that the deposited Iron bonds with the Selenium to give a rectangular lattice reconstruction on the surface; in this case, the atom whose rectangular lattice we see would be the Selenium ones. A previous STM study already mentioned in Chapter 1.4 [25] shows a similar situation to the one pondered here; the rectangular lattice constant measured in the paper refers to Se-Se interatomic distances, and amounts to 3.8 Å. In this picture, single layers of Iron and Selenium would stack on top of each other to compose the islands [14]; also, the lattice constant would be the same for both layers, i.e. suggesting a distance between Iron nearest neighbors of 3.8 Å. This value is the one closest to the measured 3.5 Å, which has been found to be constant investigating different islands. We found that the orientation of the lattice changes over the sample: Figure 4.19 shows two rectangular lattices tilted of about 30°. Analyzing the cross section of the image, the same height for the two lattices results, suggesting that they either belong to the same island, or belong to two merging islands.

On the sample, other analysis have been performed, such as Scanning Tunneling Spectroscopy (STS) and Low Energy Electron Diffraction (LEED). For the STS, different acquisitions in different points of an island have been made, sweeping the voltage from 30 mV to −30 mV, and recording the dI/dU characteristic. The scope of this measurement was to investigate the presence
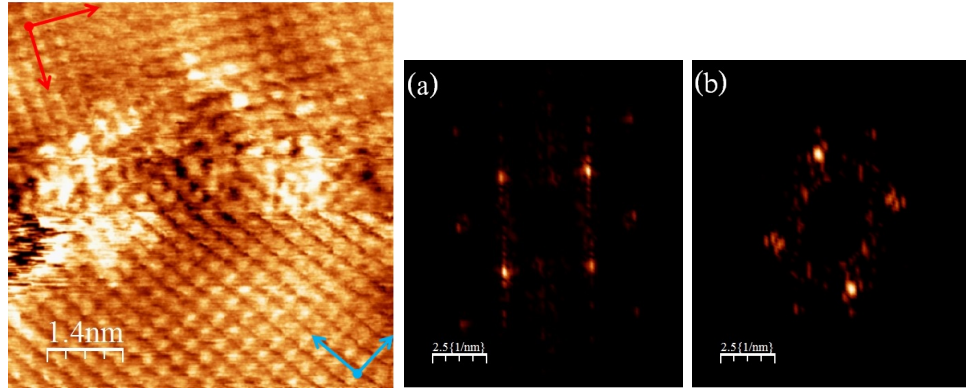
Figure 4.20: Fe on Bi_2Se_3. Quasi-costant height image showing two rectangular lattices on the surface with two different orientations (the arrows are a guide for the eyes). The FFTs show the change in the periodicity of the lattice between the lower part of the image (a), and the upper part of the image (b). Images' size 7×7 nm^2. $I = 600$ pA, $U = 170$ mV.

of a gap in the conductive feature, which is peculiar of the superconductive state. Furthermore, a superconductive gap would strongly indicate that the islands actually consists of FeSe, which holds superconductive properties. Unfortunately the STS has revealed no gap, showing a metallic behavior; this result agrees with others [14] [19] who claim the superconductive transition temperature to be approximately 8 K for the FeSe. However, it has to be pointed out that, since different conditions and procedures for samples' preparation can change their physical and chemical properties, it is impossible to determine the evolution of the T_C beforehand. On the other hand, the LEED investigation was extremely hurdled due to the macroscopic roughness of the sample, which blocked the diffractive phenomenon. As previously explained the Bi_2Se_3 is produced in scales and then cleaved with a scotch tape; often occurs that the cleaved surface is not macroscopically flat, but is nonetheless possible to probe the sample on a microscopical area with the STM.

To summarize, no growing of Holmium islands has been observed neither on the Iridium (111) nor on the Platinum (111) surface. In both cases the Holmium tends to form clusters rather than islands, and a peculiar behavior of its atoms on the surfaces is observed. In addition it has been made clear how the clusters size depend on the thermal energy, by means of annealing the
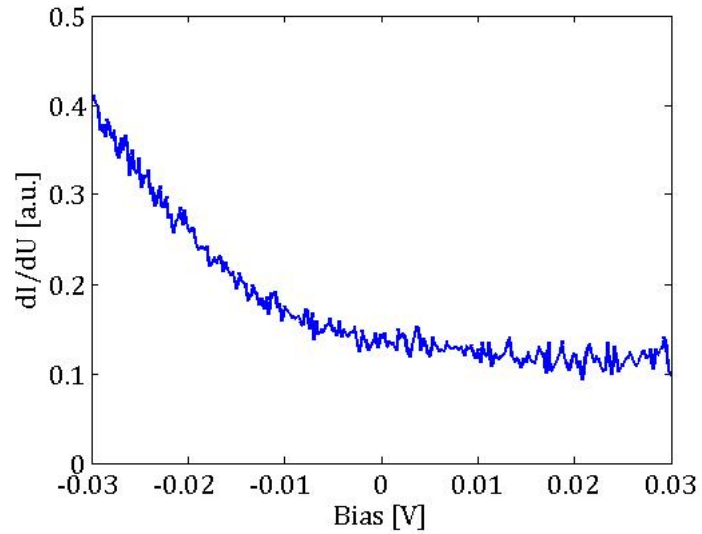
Figure 4.21: Fe on Bi_2Se_3. Spectroscopy on top of an atom belonging to the rectangular lattice. No superconductive feature is present in the graph.

sample, or cold depositing the Holmium. On the other hand, deposited Iron on Bismuth Selenide forms smooth islands, whose nature and composition is still unclear, and needs further investigation. The island showed a rectangular reconstruction, in contrast to the exagonal lattice characteristic of the Bi_2Se_3; the lattice constant has found to be similar to the one of the FeSe, though no evidence of superconductivity emerged.

Chapter 5

Holmium distribution statistical analysis

This chapter explains the analysis I have done on the Holmium atom distribution on top of both Iridium(111) and Platinum(111). The scope of the analysis is to achieve a better comprehension of the Holmium atoms distribution on the surface, and to understand if there is an underlying order behind it. I used a Matlab code written by the research group of Hamburg, and compared the result with some measurements obtained thanks to the program WSxM. First the theoretical approach and the modus operandi of the program is clarified, then the results are presented followed by a short discussion. Further insights on the theory here presented can be found in [4][8].

5.1   Statistical theory

The key idea is to extract a function, namely the pair correlation function, that can provide information about the distribution of the atoms on the surface; in particular it is interesting to understand whether such a function is a random one or presents any characteristic feature. The pair correlation function is a well known statistical quantity, and can be extracted, after due normalization, from STM topographies.

The pair correlation function can be defined for a two-dimensional system and in the canonical ensemble, which has the temperature T, the surface A and the particle number N as natural variables. The partition function

53

associated to this system is defined as follows, introducing the inverse temperature $\beta = 1/k_B T$ and the expression $\mathbf{r}^N$, that denotes the $2N$-dimensional vector containing the positions $\mathbf{r}_1 = (x_1, y_1), \mathbf{r}_2 = (x_2, y_2), ..., \mathbf{r}_N = (x_N, y_N)$ of all N particles, and the potential energy $V(\mathbf{r}^N)$ for this configuration:

$$Z_N(A, T) = \int d\mathbf{r}_1...d\mathbf{r}_N e^{-\beta V(\mathbf{r}^N)} = \int d\mathbf{r}^N e^{-\beta V(\mathbf{r}^N)}. \tag{5.1}$$

The probability density to find a particle 1 at $\mathbf{r}_1$, particle 2 at $\mathbf{r}_2$, etc. can be derived from $Z_N(A, T)$:

$$P_N^{(N)}(\mathbf{r}^N) = \frac{e^{-\beta V(\mathbf{r}^N)}}{Z_N(A, T)}. \tag{5.2}$$

In principle, all state variables can be determined from the partition function. However, it is beneficial to take only a subset of $n \ll N$ particles into account. In that case an n-body probability density can be calculated by integrating over the coordinates of the remaining $N - n$ particles:

$$P_N^{(n)}(\mathbf{r}_1, ..., \mathbf{r}_n) = \int P_N^{(n)}(\mathbf{r}^N) d\mathbf{r}_{n+1}...d\mathbf{r}_N \tag{5.3}$$

The correlation between different particles decreases with their relative separation. In the limit of infinite distances between pairs of particles, they behave completely uncorrelated and the n-particle probability density factorizes into a product of n single-particle probability densities:

$$P_N^{(n)}(\mathbf{r}_1, ..., \mathbf{r}_n) = \prod_{i=1}^{n} P_N^{(1)}(\mathbf{r}_i). \tag{5.4}$$

The n-particle distribution function is defined as the ratio between correlated and uncorrelated n-particle probability densities. Hence that quantity can be understood as a deviation from an ideal gas-like behavior:

$$g_N^{(n)}(\mathbf{r}_1, ..., \mathbf{r}_n) = \frac{P_N^{(n)(\mathbf{r}_1,...,\mathbf{r}_n)}}{\prod_{i=1}^{n} P_N^{(1)(\mathbf{r}_i)}}. \tag{5.5}$$

For $n = 2$ it is called the pair distribution function or pair correlation function:

$$g_N^{(2)}(\mathbf{r}_1, \mathbf{r}_2) = \frac{P_N^{(2)}(\mathbf{r}_1, \mathbf{r}_2)}{P_N(1)(\mathbf{r}_1) P_N^{(1)}(\mathbf{r}_2)}. \tag{5.6}$$

In the following we will assume the thermodynamic limit with $N, V \to \infty$. The index N and the superscript (2) are dropped, and the pair correlation function is reduced to $g(\mathbf{r}_1, \mathbf{r}_2)$. From the definition of the pair correlation function it follows $g(\mathbf{r}_1, \mathbf{r}_2) \geq 0$. In the limit $\mathbf{r}_1 - \mathbf{r}_2 \to \infty$, the uncorrelated behavior leads to $g(\mathbf{r}_1, \mathbf{r}_2) \to 1$. In the case of a spatially homogeneous system, $g(\mathbf{r}_1, \mathbf{r}_2)$ depends only on the relative separation of two particles, $g(\mathbf{r}) = g(\mathbf{r}_1 - \mathbf{r}_2)$. In the case of an isotropic system, it could be further simplified to $g(r) = g(|\mathbf{r}_1 - \mathbf{r}_2|)$. Albeit, this is not the case of Ho on Ir(111)/Pt(111), due to the non-isotropic variation of the adsorption potential, it is still very useful to evaluate the isotropic pair distribution function. In addition, the knowledge of the $g(r)$ carries also information about the quantity $w(r)$, defined as

$$w(\mathbf{r}_1, \mathbf{r}_2) = -k_B T \ln g(\mathbf{r}_1, \mathbf{r}_2). \qquad (5.7)$$

Such a quantity, at T, N, and A constant equals the work required to pull two particles close together from an infinite distance to a relative distance $r = r_1 - r_2$, and it is useful for the further analysis. It is important to notice that $w(r)$ is not the pure potential linking two particles, usually called pair potential, but an effective potential $V_{eff}(r)$ that takes into account also the presence of the surrounding particles.

The following explains how the pair distribution function $g(r)$ is evaluated from the experimental data at hand. The first step is to locate the position of the Holmium adatoms on the surface, without taking into account the clusters. The topographies are multidimensional matrices that for every point (x, y) record a value of the height z and are then represented as height color maps, whose contrast scale is set after the minimum and maximum z values. By importing these matrices in the Matlab environment, is possible to extract the position of the adatoms. To do so the Matlab code is implemented in a manner that, given an STM topography, permits to extract the position of the adatoms in the image by using a cross-hair cursor. Hence, every position is stored in a table reporting the coordinates of every selected adatom. Every position is expressed as (x, y) pixel coordinates, which directly corresponds to coordinates in nanometers. Being the size of the images used for this analysis 40×40 nm^2, and 512×512 px^2 their resolution, the uncertainty in the position is $\Delta x = \Delta y = 40$ nm/512 px ≈ 0.8 Å. A distance histogram with atom-atom distances for a particular topography is generated by taking all combinations of atoms into account up to a particular range of interest (i.e.
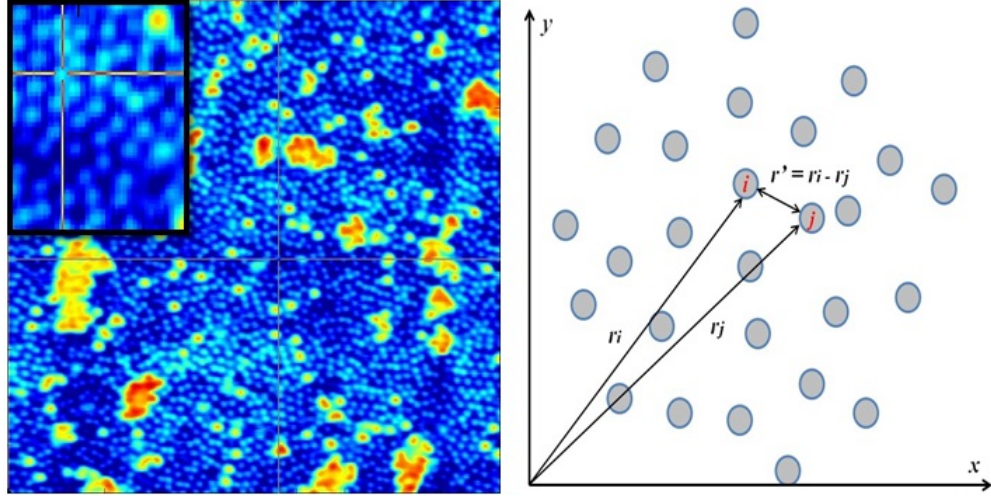
Figure 5.1: Left: One of the topographies used for the analysis introduced in the Matlab environment; in the inset is shown the hairy cursor to select the atoms. Note that the underlying substrate's atom cannot be seen. Right: Schematic of how the autocorrelation function works; the circles ideally represent the Holmium adatoms on a substrate.

interactions are supposed to be negligible for atoms farther than 15 nm away from each other). The histogram can be easily expressed by the formula

$$f(r) = \sum_{i}^{N} \sum_{j=1j\neq i}^{N} \delta_{rr'} \qquad (5.8)$$

where $r' = r_i - r_j$ is the displacement of all surrounding atoms (j) with respect to a given atom (i), for all atoms in the image. This means that for any given adatom (i) the displacement to the other adatoms is evaluated. Then the procedure is repeated for every atom (i), and the values of the displacement are split and classified on the basis of r. The precision set for the histogram, and for the further analysis, is set to 1 Å, since it is the lowest limit above the uncertainty in the position of the atoms. In order to obtain the pair correlation function, the distribution function $f(r)$ has to be normalized by a statistical random distribution. In our case a random distribution $f_{ran}(r)$ can be obtained from randomly generated distributions of Ho atoms with the same number of Ho atoms and the same area as in the experimental data. A similar histogram is build in the same fashion as

the $f(r)$. The ratio of $f(r)$ and $f_{ran}(r)$ equals the pair correlation function $g(r) = f(r)/f_{ran}(r)$, in accordance with its definition $g_N^{(2)}(\mathbf{r}_1, \mathbf{r}_2)$. Once the $g(r)$ is given, the also isotropic $V_{eff}(r)$ is easily obtained from the formula (5.7).

5.2   Results and Discussion

I have analyzed on both Ir(111) and Pt(111) an overall area of 80×80 nm^2, counting a total of about 3600 atoms on the Iridium and 1000 on the Platinum. By definition, the histogram shows the calculated incidence of distances between the atoms, and thus, the higher the peak, the more probable the distance is. Furthermore, these peaks corresponds to minima in the effective potential characteristic, that can be seen as equilibrium positions in the atom distribution. In Figure 5.2 a comparison between the $g(r)$ and the effective potential for the two cases is shown. As one could already see from the topographies, the Holmium seems to be more ordered on the Iridium, despite the presence of clusters; the pair distribution histogram shows a narrower peak, compared to the Platinum one, suggesting a more defined average distance between the atoms, and the presence of a minimum, which indicates that certain distances are somehow forbidden. The potential in blue line in Figure 5.2 shows two minima in the range 0-2 nm, which in principle can be thought as the position of the *1st* and *2nd* nearest neighbor Holmium adatom. The position of these minima has been compared to the distances measured with the program WSxM on particularly ordered spots in the topographies. In doing so, the distance between the Ho atoms on Ir(111) is measured along a row of atoms, as shown in the cross section below. Also, a schematic exagonal lattice has been superimposed on particular well ordered spots on the image, highlighting a short range order; the lattice fits the atom distribution up to the second nearest neighbor Ho adatom (Figure 5.3). A good match is found around the value of $r = 8.5$ Å between the above measurements (lattice and cross-section) and the position of the first minimum in the $V_{eff}(r)$ characteristic. Also, there is a good agreement between the position of the other minimum and the measured distance of the second nearest neighbor adatom, as shown in Figure 5.4. Moreover, the broadening of the second minimum is a clear index of how the degree of order decreases after the first nearest neighbor.

Another angle that is worth to point out is that both substrates show a
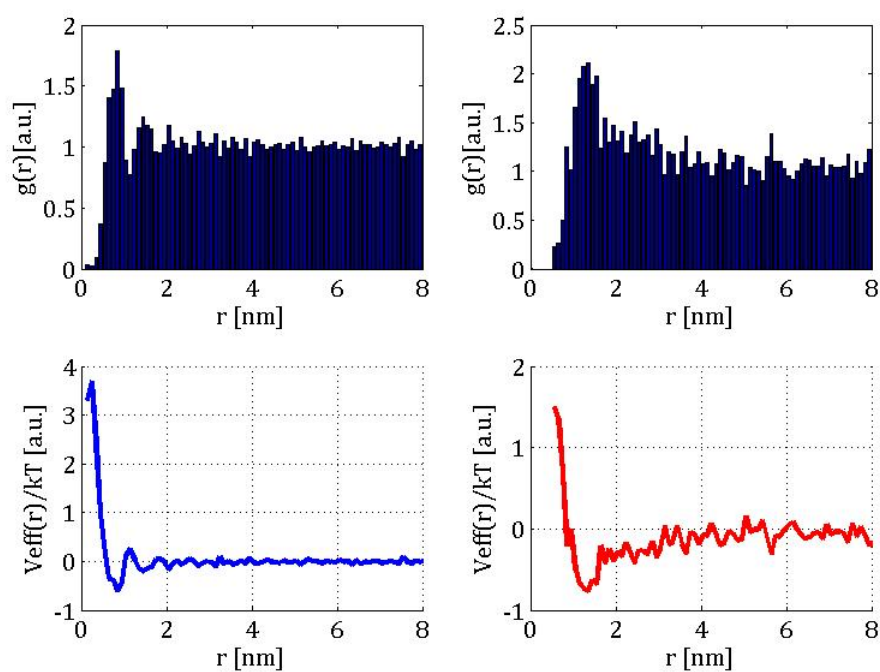
Figure 5.2: Left panels: Ho/Ir(111) $g(r)$ and potential (blu line). Right panels: Ho/Pt(111) $g(r)$ and potential (red line).
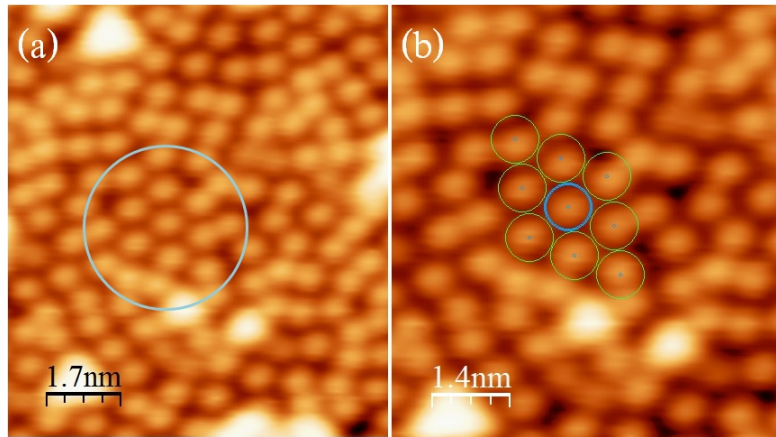
Figure 5.3: Ho adatoms on Ir(111). In Figure (a) is highlighted a ordered arrangement of adatoms. (b) on the adatoms arrangement is superimposed an exagonal lattice through the program WSxM. The lattice constant is 0.855 nm.
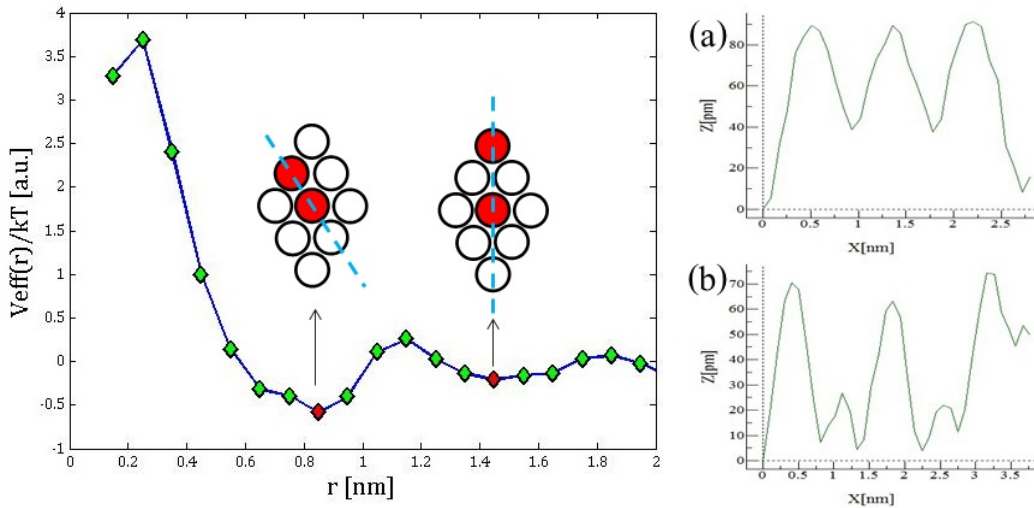
Figure 5.4: Positions of the 1*st* and 2*nd* n.n. Ho adatom on Ir(111). The graph shows a zoom of the potential in the range from 0 to 2 nm. The position of the two minima is highlighted in red on the graph. (a) cross section along the direction depicted in the first inset on the graph; shows the distance between three first nearest neighbors. (b) cross section along the direction depicted in the second inset; shows the distance between three second nearest neighbor.

Figure 5.5: Holmium on Platinum at different temperatures. (a) Comparison of the two effective potential calculated for the deposition at room temperature (red line) and for the deposition at $-180°$ C(magenta line). (b) Zoom on the range from 0 to 2 nm; the minimum for the magenta line is shifted to smaller distances.

strong peak in the pair correlation functions (Figure 5.2), but at different distances; moreover, the peak position is gre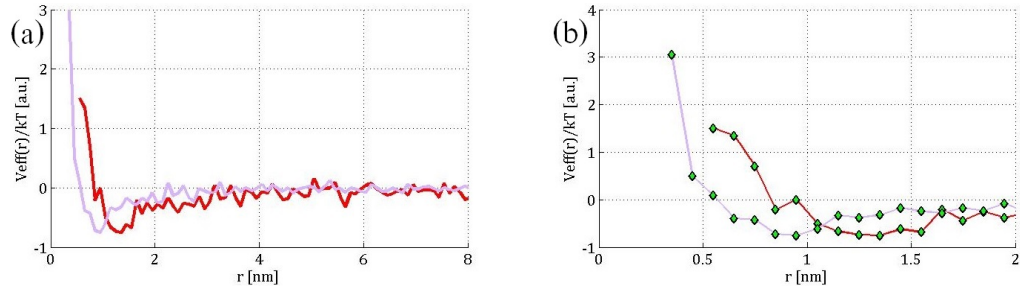ater for the Platinum, helping to explain the lower count of atoms compared to the Iridium case. Along this topic, it is useful to look deeper into the Platinum analysis. For the Platinum, two images of 40×40 nm^2 were taken, one corresponding to the room temperature Holmium deposition, and the other corresponding to the cold deposition. Comparing the two potentials (the minima in the $g(r)$ correspond to the maxima in the potential and vice versa) in Figure 5.5, one can see that the position of the minima is lower in the case of the cold deposition, suggesting a lower atom-atom distance. This feature is also confirmed by the counts in the two cases: 360 Ho atoms for the room temperature deposition, and 720 atoms for the cold deposition. It is also interesting to note how this behavior is linked to the decreased number of clusters (Chapter 4.2), which is due to a low thermal energy contribution during the cold deposition.

At last, a few things can be said about the repulsion between the adatoms. Most certainly, this is a puzzling feature because the substrates, as well as the deposited material, are metals, whereas this kind of repulsion is expected to be found among charged particles. A few examples for the latter case regard the repulsion and consecutive ordering of deposited molecules on a substrate [7][29]. On the other hand, is well known in literature the case of Cu adatoms on the Cu(111) surface where a screening between the adatoms has been discovered. Such behavior has to be ascribed to the surface state Friedel oscillations, that mediate the interaction between the adatoms

[22][18]. For our case, however, this possible explanation has to be ruled out, since neither Iridium nor Platinum possess similar surface states. With our present result we can only hypothesize a coulombian nature of the effect.

To summarize, the Holmium atoms seem to feel a stronger interaction with each other on the Iridium rather than on the Platinum, and this leads to a higher degree of order as shown in the topography images and confirmed with the statistical analysis. In addition, the temperature effect is to decrease the interatomic distance, at least on the Platinum. Finally, there is a good agreement around the value of 8.5 Å on the interatomic distance in the Ho/Ir(111) case, and an estimate of the value of the isotropic $V_{eff}(r)$ is possible. However it is important to point out the limits of this analysis, which has to be seen as a starting point rather than a conclusion. Firstly, a complete statistical analysis needs a greater set of data and topographies images to rule out the influence of noise and other biasing factors. Secondly, the data set could be improved further by removing the clusters also in the more interesting case of Ho/Ir(111); for this purpose, a cold deposition seems to be the easiest way, in my experience. Finally, this analysis was performed considering just the isotropic perspective due to the short range order. In case of long range order, a 2D-vector analysis would have been possible, ultimately pursuing a better understanding of the nature of this particle interaction.

Chapter 6

Summary and outlooks

In this thesis growth of novel materials on surfaces for advanced technology were investigated by scanning tunneling microscopy. On one hand Holmium, a material with interesting magnetic properties, was deposited and studied after being deposited on highly conductive metals as the Platinum and the Iridium. Then, we have inquired into the growth and interaction of Iron with Bismuth Selenide as a topological insulator, especially looking for the formation of Iron Selenide, a well known high T_C superconductor.

In the framework of my study Holmium has been observed to grow without forming islands onto clean Iridium (111) and Platinum (111) surfaces. The deposited Holmium has shown a tendency to form clusters whose size has been proven to change depending on the temperature deposition, for the case of the Platinum, and depending on annealing temperatures, on Iridium; in particular, a temperature raise favors the aggregation of atoms to form larger clusters. This study has also shown a fascinating behavior of Holmium adatoms on the substrate in the sub-monolayer regime; the adatoms arrange on the surface distant from each other as if under a repulsive interaction. A further statistical investigation supported by the use of a Matlab program has highlighted a short range order for the Holmium adatoms in the case of the deposition on Iridium, while a lower ordering tendency has appeared on the Platinum. In the first case Holmium adatoms arrange in hexagonal patches with nearest neighbors interatomic distance of about 0.85 nm. These findings have been strengthened by the good match between the experimental measure of the patches interatomic distances through the topographies, and the average value calculated by means of the statistical analysis. As far as concerning the causes behind such ordering, additional studies are required;

in particular, the realization of a sample with a longer range order would allow to develop further the statistical analysis, as showed in [20]. Also, could be interesting to deposit Holmium on other substrates, so to understand if its peculiar behavior has to be ascribed to the material itself, or to its interaction with the substrates at hand.

Iron has been deposited at room temperature on the Bismuth Selenide's sample, that has been annealed right afterwards: on the surface's top, smooth islands have been found with an average area of about 20×20 nm^2, whose composition is still unclear. Some of the probed islands presented a rectangular lattice on their topmost layer, which is in utter contrast with a pseudomorphical growth of the Iron. A valid hypothesis would suggest a coalescence of the deposited Iron and the Selenium topmost layer into forming FeSe islands; a fair match is found between the measured lattice parameter 3.5 Å and the literature's one for the FeSe, 3.8 Å. Single point scanning tunneling spectroscopy measurements have been performed on these islands at 30 K, but no superconducting gap was found. A considerable improvement of this analysis could be the evaluation of the islands' spectroscopic features at cryogenic temperatures below the acknowledged superconducting temperature of the FeSe. Albeit no final conclusion can be taken after this study, great interest dwells in the synthesis of the FeSe by simple MBE deposition of Iron. Furthermore, exciting features could arise by the combination of a simple novel superconductor as the Iron Selenide and the topological insulator Bismuth Selenide.

Bibliography

[1] H. Binning, G., Rohrer. Si 7x7 reconstruction. *Physical Review Letters*, 50(2), 1983.

[2] Harald Brune, Marcella Giovannini, Karsten Bromann, and Klaus Kern. Self-organized growth of nanostructure arrays on strain-relief patterns. 394(July):451–453, 1998.

[3] C. Busse, S. Baud, G. Bihlmayer, C. Polop, T. Michely, and S. Blügel. Tunneling voltage dependent heights of faulted and unfaulted Ir islands on Ir(111). *Physical Review B*, 68(20):201401, November 2003.

[4] D Chandler. *Introduction to Modern Statistical Mechanics*. Oxford University Press, 1987.

[5] C. Julian Chen. *Introduction to Scanning Tunnegling Microscopy*. Oxford University Press, second edition, 2007.

[6] T Eelbo, M Sikora, G Bihlmayer, M Dobrzaski, a Kozowski, I Miotkowski, and R Wiesendanger. Co atoms on Bi 2 Se 3 revealing a coverage dependent spin reorientation transition. *New Journal of Physics*, 15(11):113026, November 2013.

[7] I. Fernandez-Torrente, S. Monturet, K. Franke, J. Fraxedas, N. Lorente, and J. Pascual. Long-Range Repulsive Interaction between Molecules on a Metal Surface Induced by Charge Transfer. *Physical Review Letters*, 99(17):176103, October 2007.

[8] J P Hansen and I R McDonald. *Theory of Simple Liquids*. Elsevier Science, 2006.

[9] M. Z. Hasan and C. L. Kane. Colloquium: Topological insulators. *Reviews of Modern Physics*, 82(4):3045–3067, November 2010.

[10] D Haude. *Rastertunnelspektroskopie auf der InAs(110)-Oktoberflache: Untersuchungen an drei-, zwei- und nulldimendsionalen Elektronensystemen im Magnetfeld.* PhD thesis, University of Hamburg, 2001.

[11] Stefan Heinze, Kirsten von Bergmann, Matthias Menzel, Jens Brede, André Kubetzka, Roland Wiesendanger, Gustav Bihlmayer, and Stefan Blügel. Spontaneous atomic-scale magnetic skyrmion lattice in two dimensions. *Nature Physics*, 7(9):713–718, July 2011.

[12] Michael Hohage, Thomas Michely, and George Comsa. Pt(111) network reconstruction: structure, growth and decay. *Surface Science*, 337(3):249–267, September 1995.

[13] J. Honolka, a. a. Khajetoorians, V. Sessi, T. O. Wehling, S. Stepanow, J.-L. Mi, B. B. Iversen, T. Schlenk, J. Wiebe, N. B. Brookes, a. I. Lichtenstein, Ph. Hofmann, K. Kern, and R. Wiesendanger. In-Plane Magnetic Anisotropy of Fe Atoms on Bi_{2}Se_{3}(111). *Physical Review Letters*, 108(25):256811, June 2012.

[14] Fong-Chi Hsu, Jiu-Yong Luo, Kuo-Wei Yeh, Ta-Kun Chen, Tzu-Wen Huang, Phillip M Wu, Yong-Chi Lee, Yi-Lin Huang, Yan-Yi Chu, Der-Chung Yan, and Maw-Kuen Wu. Superconductivity in the PbO-type structure alpha-FeSe. *Proceedings of the National Academy of Sciences of the United States of America*, 105(38):14262–4, September 2008.

[15] Bardeen J. Tunneling from a many-particle point of view. 6(2):6–8, 1961.

[16] C Jensen and U Ko. Structure and growth of holmium on W (110). 456:712–718, 2000.

[17] Sunghun Kim, M. Ye, K. Kuroda, Y. Yamada, E. E. Krasovskii, E. V. Chulkov, K. Miyamoto, M. Nakatake, T. Okuda, Y. Ueda, K. Shimada, H. Namatame, M. Taniguchi, and a. Kimura. Surface Scattering via Bulk Continuum States in the 3D Topological Insulator Bi_{2}Se_{3}. *Physical Review Letters*, 107(5):056803, July 2011.

[18] N. Knorr, H. Brune, M. Epple, a. Hirstein, M. Schneider, and K. Kern. Long-range adsorbate interactions mediated by a two-dimensional electron gas. *Physical Review B*, 65(11):115420, March 2002.

[19] Hisashi Kotegawa, Satoru Masaki, Yoshiki Awai, Hideki Tou, Yoshikazu Mizuguchi, and Yoshihiko Takano. Evidence for Unconventional Superconductivity in Arsenic-Free Iron-Based Superconductor FeSe: A 77 Se-NMR Study. *Journal of the Physical Society of Japan*, 77(11):113703, November 2008.

[20] P. Löptien, L. Zhou, J. Wiebe, a. a. Khajetoorians, J. L. Mi, B. B. Iversen, Ph. Hofmann, and R. Wiesendanger. Screening and atomic-scale engineering of the potential at a topological insulator surface. *Physical Review B*, 89(8):085401, February 2014.

[21] Toshio Miyamachi, Tobias Schuh, Tobias Märkl, Christopher Bresch, Timofey Balashov, Alexander Stöhr, Christian Karlewski, Stephan André, Michael Marthaler, Martin Hoffmann, Matthias Geilhufe, Sergey Ostanin, Wolfram Hergert, Ingrid Mertig, Gerd Schön, Arthur Ernst, and Wulf Wulfhekel. Stabilizing the magnetic moment of single holmium atoms by symmetry. *Nature*, 503(7475):242–6, November 2013.

[22] J Repp, F Moresco, G Meyer, K H Rieder, P Hyldgaard, and M Persson. Substrate mediated long-range oscillatory interaction between adatoms: Cu /Cu(111). *Physical review letters*, 85(14):2981–4, October 2000.

[23] Niklas Romming, Christian Hanneken, Matthias Menzel, Jessica E Bickel, Boris Wolter, Kirsten von Bergmann, André Kubetzka, and Roland Wiesendanger. Writing and deleting single magnetic skyrmions. *Science (New York, N.Y.)*, 341(6146):636–9, August 2013.

[24] T. Schlenk, M. Bianchi, M. Koleini, a. Eich, O. Pietzsch, T. Wehling, T. Frauenheim, a. Balatsky, J.-L. Mi, B. Iversen, J. Wiebe, a. Khajetoorians, Ph. Hofmann, and R. Wiesendanger. Controllable Magnetic Doping of the Surface State of a Topological Insulator. *Physical Review Letters*, 110(12):126804, March 2013.

[25] Can-Li Song, Yi-Lin Wang, Peng Cheng, Ye-Ping Jiang, Wei Li, Tong Zhang, Zhi Li, Ke He, Lili Wang, Jin-Feng Jia, Hsiang-Hsuan Hung, Congjun Wu, Xucun Ma, Xi Chen, and Qi-Kun Xue. Direct observation of nodes and twofold symmetry in FeSe superconductor. *Science (New York, N.Y.)*, 332(6036):1410–3, June 2011.

[26] a. Sonntag, J. Hermenau, a. Schlenhoff, J. Friedlein, S. Krause, and R. Wiesendanger. Electric-Field-Induced Magnetic Anisotropy in a Nanomagnet Investigated on the Atomic Scale. *Physical Review Letters*, 112(1):017204, January 2014.

[27] D R Tersoff, J, Hamann. Theory of the scanning tunneling microscope. 31(2), 1985.

[28] D R Tersoff, J, Hamann. Theory and Application for the Scanning Tunneling Microscope. 50(25):1998–2001, 1998.

[29] J Trost, T Zambelli, J Wintterlin, and G Ertl. Adsorbate-adsorbate interactions from statistical analysis of STM images: N/Ru(0001). *Physical review. B, Condensed matter*, 54(24):17850–17857, December 1996.

[30] A Wachowiak. *Aufbau einer 300mK-Ultrahochvakuum/Rastertunnelmikroskopie- Anlage mit 14 Tesla Magnet und spinpolarisierte Rastertunnelspektroskopie an ferromagnetischen Fe.* PhD thesis, University of Hamburg, 2003.

[31] Li-jun Wan, Masanori Hara, Jungi Inukai, and Kingo Itaya. In Situ Scanning Tunneling Microscopy of Well-Defined Ir (111) Surface : High-Resolution Imaging of Adsorbed Sulfate. (111):6978–6983, 1999.

[32] E Weschke, H Ott, R Meier, G Kaindl, D V Vyalikh, Chandan Mazumdar, C Sutter, D Abernathy, and G Grubel. Resonant magnetic X-ray scattering from ultrathin Ho metal films down to a few atomic layers. 116:953–957, 2001.

[33] E. Weschke, H. Ott, E. Schierle, C. Schüß ler Langeheine, D. Vyalikh, G. Kaindl, V. Leiner, M. Ay, T. Schmitte, H. Zabel, and P. Jensen. Finite-Size Effect on Magnetic Ordering Temperatures in Long-Period Antiferromagnets: Holmium Thin Films. *Physical Review Letters*, 93(15):157204, October 2004.

[34] R Wiesendanger. *Scanning Probe Microscopy and Spectroscopy: Methods and Applications.* Scanning Probe Microscopy and Spectroscopy: Methods and Applications. Cambridge University Press, 1994.

[35] Qi-Hui Wu. A new (33) R 40 surface reconstruction of the Pt(111) surface. *Philosophical Magazine Letters*, 93(8):465–472, August 2013.

[36] M. Ye, S. V. Eremeev, K. Kuroda, E. E. Krasovskii, E. V. Chulkov, Y. Takeda, Y. Saitoh, K. Okamoto, S. Y. Zhu, K. Miyamoto, M. Arita, M. Nakatake, T. Okuda, Y. Ueda, K. Shimada, H. Namatame, M. Taniguchi, and a. Kimura. Quasiparticle interference on the surface of Bi_{2}Se_{3} induced by cobalt adatom in the absence of ferromagnetic ordering. *Physical Review B*, 85(20):205317, May 2012.

[37] Wei Zhang, Rui Yu, Hai-Jun Zhang, Xi Dai, and Zhong Fang. First-principles studies of the three-dimensional strong topological insulators Bi 2 Te 3 , Bi 2 Se 3 and Sb 2 Te 3. *New Journal of Physics*, 12(6):065013, June 2010.